

ANALYSIS AND MEASUREMENTS OF ARBITRARILY SHAPED OPEN MICROSTRIP STRUCTURES

Z. A. Maricevic and T. K. Sarkar

- 1. Introduction**
- 2. Formulation of the Problem**
 - 2.1 Electric field integral equation
 - 2.2 Horizontal current element in microstrip
 - 2.3 Utilization of triangular basis functions
 - 2.4 Numerical simulation of a match-termination
- 3. Matrix Pencil**
- 4. Menzel's Leaky-Wave Antenna**
- 5. Experimental Verification**
 - 5.1 Microstrip device under test de-embedding
 - 5.2 Interdigital capacitor
 - 5.3 Single loop inductor
 - 5.4 Parallel-coupled-line band-pass filter
 - 5.5 Two-port resonant structures
 - 5.5.1 Gap-coupled, half-wave filter
 - 5.5.2 Gap-coupled, ring resonator disturbed by a notch
 - 5.6 Hybrid ring coupler (rat-race)
- 6. Conclusion**

1. Introduction

Printed circuit technology has revolutionalized circuit design. It has replaced a myriad of interconnecting posts and wires with a simple planar structure - a metal-laminated dielectric board that houses electronic elements on one of its sides and connects the same elements through a printed conducting foil on the other. This "printed circuit" board has good mechanical and insulating properties, is inexpensive,

and the printed interconnection pattern is easily reproduced by photolithography.

Printed circuit technology culminates in integrated circuits. The dielectric substrate is the semiconductor material itself (e.g., silicon, GaAs) in which all needed active and passive elements such as transistors, diodes, capacitors and resistors are fabricated.

In the low frequency range ($f < 100$ MHz), the interconnecting foils are very short in terms of the wavelength. However, for $f > 100$ MHz, and in particular in the microwave frequency range ($f > 300$ MHz), it becomes necessary to consider these interconnecting foils as transmission line sections. The printed circuit structure in which the bottom side of the laminated board is grounded and the top side is a signal-carrying printed strip is known as a **microstrip**. A sample cross-section and associated parameters are shown in Figure 1. The term “microstrip” and its use in microwaves was first introduced by Grieg and Engelmann of ITT laboratories [1], in 1952.

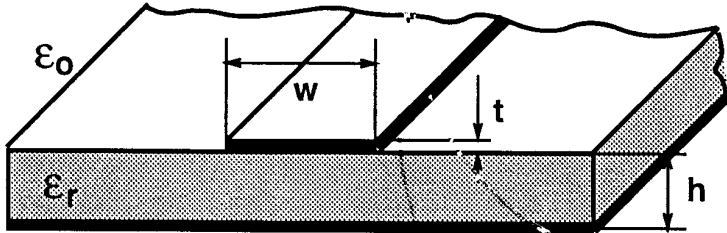


Figure 1. Parameters of a microstrip transmission line.

The main purpose of the microstrip is to be a transmission line. Due to its inhomogeneous cross-section, it can not support a simple transverse electromagnetic (TEM) wave. In general, the modes on the microstrip are hybrid, and contain longitudinal components of both the electric and the magnetic fields. However, the dielectric substrate is usually electrically very thin, yielding longitudinal components much smaller than transverse components, allowing for a quasi-TEM approximation [1]. Figure 2 shows a transversal field distribution on the microstrip.

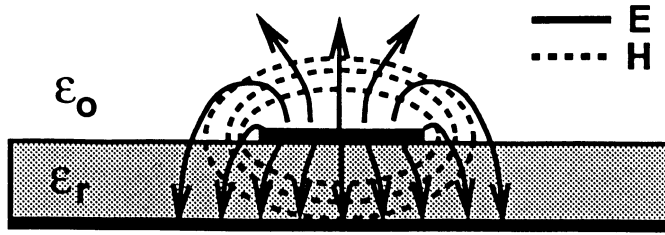


Figure 2. Cross-sectional field distribution of a microstrip transmission line.

The quasi-TEM approximation equates the transverse pattern of the electric and the magnetic fields on the microstrip with those of static case, i.e., at frequency $f = 0$ Hz, and is also known as a quasi-static approximation.

Good approximations for the characteristic impedance, phase velocity and propagation constant are obtained from values of capacitance per unit length and inductance per unit length for the static case [2]. The quasi-static approximation is valid below higher-order mode cutoff frequencies and the introduction of the radiation.

Many mathematical tools are used in obtaining the quasi-static parameters of a microstrip line: conformal mapping for the case of a zero-thickness upper conductor by Schneider [3] and Wheeler [4], finite difference method by Stinehelfer [5], integral equation (Green's function) method by Silvester [6] and Farrar and Adams [7] and the variational method in Fourier transform domain by Yamashita and Mittra [8]. The detailed description of these approaches is also given in [9] by Gupta, Garg and Bahl. The dispersion (change of microstrip properties with frequency) is not taken into account by the quasi-static approach. Both characteristic impedance (Z_0) and effective dielectric constant (ϵ_{re}) of microstrip transmission line are frequency-dependent, the dependence of the ϵ_{re} being more significant [9]. Dispersion models consider coupling between the TEM and TM (surface wave) modes [10], give an empirical relation for phase velocity versus frequency [11] or consider some waveguide structures similar to the microstrip: dielectric-loaded ridged waveguide [12] or planar waveguide [9,13].

Another large group of methods, that takes into account the hybrid nature of propagating waves, is called full-wave analysis. This is the first approach that attempts an exact description of the structure. The real hybrid modes on the microstrip are treated as a superpo-

sition of their TE and TM components, the main objective being to find the propagation constants of these modes. Denlinger [14] and Itoh and Mittra [15] pioneered this approach and it was used extensively later, in particular, for characterization of discontinuities in microstrips [16–18]. The full-wave analysis assumes only longitudinal propagation along the microstrip, thus it is better suited for enclosed microstrip problems than for the open microstrip problem.

The microstrip is an open structure. Theoretically, the electromagnetic field extends to infinity and decays as $1/r$, amounting to radiation. The radiation increases with frequency, thicker substrates and lower permittivities, and originates mostly at discontinuities [19]. Figure 3 illustrates three dominant types of radiation on microstrip: directly radiated waves, surface waves and leaky waves [20]. For a long time, radiation on the microstrip was considered only as a nuisance. Beside the losses, it introduces unwanted coupling effects on the structure. However, the radiation is the desired effect in antennas.

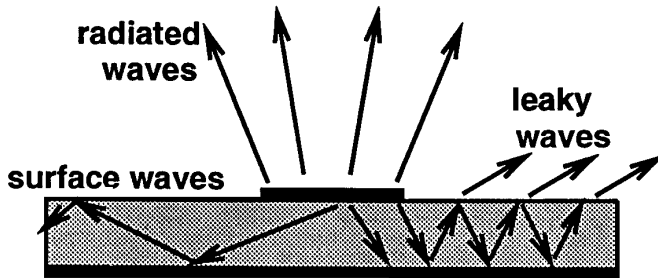


Figure 3. Three types of radiated waves on microstrip.

The microstrip antennas were introduced only in the seventies, some twenty years after the introduction of the microstrip line, and became a very popular type of antenna, due to their low profile, small size, light weight, low price and inherent microstrip suitability for large-scale production.

All the radiation effects are taken into account in a **dynamic analysis** of the microstrip. This method uses the theory of wave propagation in layered (stratified) media, first introduced by Sommerfeld in 1909. He investigated radio wave propagation above a lossy ground. His approach was extended to arbitrary stratified media much later, in 1966 by Wait [21,22] and applied to microstrip by Uzunoglu et al. [23], Mosig and Gardiol [24], Kong [25,26] and Mosig and Sarkar [27].

In this manuscript, we use the dynamic approach. In section 2, the formulation of the open microstrip problem is presented. We solve the Sommerfeld-type integral equation by the method of moments (MoM) [28,29]. In order to treat arbitrarily shaped microstrip patches, we consider triangular basis functions, first introduced by Rao [30,31]. We modify the MoM matrix in order to include the case of a match-terminated port of a microstrip device. We solve for the current distribution on the structure, and find forward and backward traveling waves on the feed lines by use of the Matrix Pencil method [32–34].

The Matrix Pencil method decomposes the current along the microstrip into a sum of complex exponentials which correspond to the modes propagating along the microstrip line. Section 3 briefly describes this method.

Section 4 presents an example of an antenna. We compare our results for Menzel’s leaky-wave antenna [35] with those of Menzel and Oliner [36,37] and demonstrate how deep insights into this problem can be obtained from use of our method.

In section 5 we present an extensive experimental verification of our method. We compare our results for scattering parameters over a wide frequency range for several two-port and four-port microstrip devices with experimental measurements, and, when possible, with results obtained by the commercial software package “Super-Compact”. All the microstrip devices shown in this section were manufactured and tested in the microwave laboratory of the Department of Electrical and Computer Engineering at Syracuse University. We also introduce an accurate de-embedding technique for elimination of test cable to microstrip connector contribution, that uses the time-domain gating option.

Section 6 summarizes the contributions of this work and presents some conclusions.

2. Formulation of the Problem

Consider an arbitrarily shaped microstrip structure as shown in Figure 4. In order to develop a compact theoretical model, we make a set of simplifying assumptions:

- the substate is a non-magnetic ($\mu = \mu_0$), homogeneous and isotropic dielectric

- both substrate and ground plane extend to infinity in (x, y) directions
- all conductors are perfect electric conductors (PEC), and have zero-thickness.

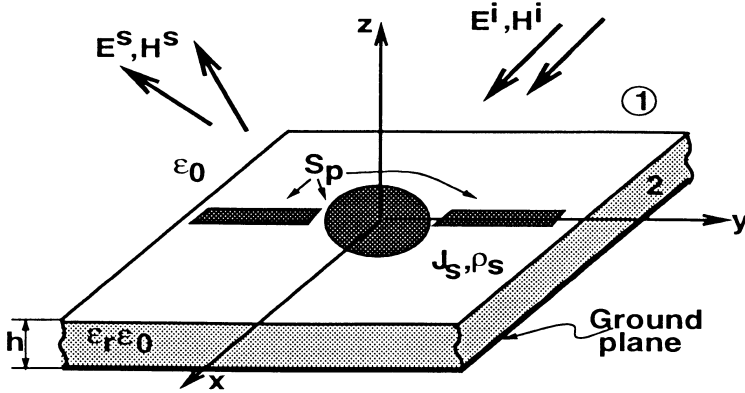


Figure 4. An arbitrarily shaped microstrip excited by impressed field $(\mathbf{E}^i, \mathbf{H}^i)$.

2.1 Electric field integral equation

The total tangential electric field on the microstrip conductor surface \mathbf{S}_p is zero, i.e.,

$$\mathbf{E}_{tan} = \hat{\mathbf{z}} \times \mathbf{E} = 0 \quad \text{on } \mathbf{S}_p \quad (1)$$

If an equivalent surface current \mathbf{J}_s on the conducting patches is assumed to exist then

$$\hat{\mathbf{z}} \times [L(\mathbf{J}_s) + \mathbf{E}^i] = 0 \quad \text{on } \mathbf{S}_p \quad (2)$$

where \mathbf{E}^i represents the excitation. (The superscript i stands for “incident” or “impressed” field). The linear operator $L(\mathbf{J}_s)$ represents the electric field produced by \mathbf{J}_s , and can be expressed as

$$L(\mathbf{J}_s) = \int \int_{\mathbf{S}_p} \bar{\bar{\mathbf{G}}}_{E|\mathbf{J}} \mathbf{J}_s ds \quad (3)$$

The term $\overline{\overline{G}}_{E|J}$ stands for the electric field modified dyadic Green's function, that includes the effects of the dielectric layer and the ground plane through the use of Sommerfeld integrals. Green's function is derived by finding the fields due to a point source, i.e., a Hertzian dipole located in the air-dielectric interface of the microstrip, as presented in the next section.

The integral equation (2) is later transformed to a matrix equation by use of Method of Moments (MoM). The solution of the matrix equation yields the surface current distribution on the microstrip.

2.2 Horizontal current element in microstrip

Consider an \hat{x} -directed horizontal electric dipole (HED) of moment $I dx$ located in the air-dielectric interface of a microstrip structure with infinite transverse directions, as shown in Figure 5. The substrate is a lossy dielectric of thickness h and complex permittivity

$$\epsilon = \epsilon_0 \epsilon_r = \epsilon_0 \epsilon'_r (1 - j \tan \delta). \quad (4)$$

Here $\tan \delta$ is the loss tangent and ϵ_r is the complex relative dielectric constant of the medium. The origin of the coordinate system is chosen to be at the location of the HED. The perfectly conducting ground plane is located at $z = -h$.

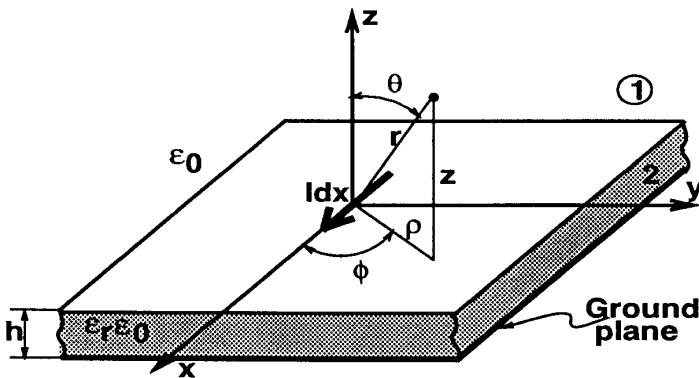


Figure 5. Horizontal electric dipole (HED) in microstrip.

We start from Maxwell's equations that, together with proper boundary conditions, completely define the fields around the micro-strip. Assuming time-harmonic fields, with complex time dependence $e^{j\omega t}$, these equations in the source-free region are

$$\nabla \times \mathbf{E} = -j\omega\mu_0\mathbf{H} \quad (5)$$

$$\nabla \times \mathbf{H} = j\omega\epsilon\mathbf{E} \quad (6)$$

$$\nabla \cdot \mathbf{E} = 0 \quad (7)$$

$$\nabla \cdot \mathbf{H} = 0. \quad (8)$$

The tangential field boundary conditions are given by

$$\hat{\mathbf{z}} \times (\mathbf{E}_1 - \mathbf{E}_2) = 0 \quad \text{at } z = 0 \quad (9)$$

$$\hat{\mathbf{z}} \times (\mathbf{H}_1 - \mathbf{H}_2) = \mathbf{J}_s \quad \text{at } z = 0 \quad (10)$$

$$\hat{\mathbf{z}} \times \mathbf{E}_2 = 0 \quad \text{at } z = -h \quad (11)$$

$$\hat{\mathbf{z}} \times \mathbf{H}_2 = \mathbf{J}_{sg} \quad \text{at } z = -h \quad (12)$$

where subscripts 1 and 2 refer to media 1 and 2, as shown in Figure 4. The normal components of magnetic field \mathbf{H} are continuous at both the $z = -h$ and $z = 0$ boundaries. We take the effect of the source element $Id\mathbf{x}$ into account in the boundary conditions, since it is located at the $z = 0$ boundary. This surface current is given by Dirac's delta-function

$$\mathbf{J}_s = \hat{\mathbf{x}}\delta(\mathbf{r})\mathbf{I}d\mathbf{x}. \quad (13)$$

It is convenient to express fields in terms of the magnetic vector potential \mathbf{A} and the scalar potential V :

$$\mathbf{E} = -j\omega\mathbf{A} - \nabla V \quad (14)$$

$$\mathbf{H} = \frac{1}{\mu_0}\nabla \times \mathbf{A} \quad (15)$$

The vector potential \mathbf{A} is not completely specified by its curl only (15). Its divergence is conveniently given in terms of scalar potential V by the Lorentz gauge [38]

$$\nabla \cdot \mathbf{A} = -j\omega\epsilon\mu_0 V. \quad (16)$$

It is then easy to show that potentials \mathbf{A} and V satisfy Helmholtz's equations [38]

$$\nabla^2 \mathbf{A} + k^2 \mathbf{A} = 0 \quad (17)$$

$$\nabla^2 V + k^2 V = 0 \quad (18)$$

and that rectangular components of \mathbf{A} also satisfy the scalar Helmholtz equation. k is the medium wave number and $k^2 = \omega^2 \epsilon \mu_0$.

In order to satisfy boundary conditions (9) – (12), two components of magnetic vector potential, A_x and A_z , are needed. The boundary conditions (9) – (12) are transformed to

$$V_1 = V_2 \quad \text{at} \quad z = 0 \quad (19)$$

$$\mathbf{A}_1 = \mathbf{A}_2 \quad \text{at} \quad z = 0 \quad (20)$$

$$\frac{\partial A_{x1}}{\partial z} - \frac{\partial A_{x2}}{\partial z} = -\mu_0 J_x \quad \text{at} \quad z = 0 \quad (21)$$

$$V_2 = 0 \quad \text{at} \quad z = -h \quad (22)$$

$$A_{x2} = 0 \quad \text{at} \quad z = -h \quad (23)$$

$$\frac{\partial A_{z2}}{\partial z} = 0 \quad \text{at} \quad z = -h \quad (24)$$

It is, however, necessary to take into account one more boundary condition, namely Sommerfeld's radiation condition

$$\lim_{r \rightarrow \infty} r \left(\frac{\partial \Psi}{\partial r} + jk\Psi \right) = 0 \quad (25)$$

where Ψ is any scalar solution to Helmholtz's equation. The physical meaning of this condition is that all solutions to the scalar Helmholtz equation represent waves traveling away from the source and decreasing in amplitude with the distance.

Since all boundary conditions appear for $z = \text{constant}$, it is appropriate to choose the cylindrical coordinate system for the microstrip problem [38,39]. In this system, Helmholtz's equation can be solved through separation of variables. The Laplacian in equation (18) has to be written in cylindrical coordinates, yielding the scalar Helmholtz equation in cylindrical coordinates

$$\frac{1}{\rho} \frac{\partial}{\partial \rho} \left(\rho \frac{\partial \Psi}{\partial \rho} \right) + \frac{1}{\rho^2} \frac{\partial^2 \Psi}{\partial \phi^2} + \frac{\partial^2 \Psi}{\partial z^2} + k^2 \Psi = 0. \quad (26)$$

A solution has the form

$$\begin{aligned} \Psi(\rho, \phi, z) = \sum_{n=0}^{\infty} H_n^{(2)}(k_\rho \rho) (A_n e^{jk_z z} + B_n e^{-jk_z z}) \times \\ (C_n \sin(n\phi) + D_n \cos(n\phi)) \end{aligned} \quad (27)$$

where $H_n^{(2)}$ is the n^{th} order Hankel function of the second kind that also satisfies the condition (25). The constants A_n, B_n, C_n and D_n are to be determined from the other boundary conditions, and the ρ and z -directed complex “propagation constants” k_ρ and k_z are related by

$$k_\rho^2 + k_z^2 = k^2 = \omega^2 \epsilon \mu_0. \quad (28)$$

The general solution is the integration of Ψ over either spectral variable k_ρ or k_z . Taking into account the nature of Ψ , the integration over k_ρ leads to Hankel transforms and is better suited for this axially symmetrical problem than integration over k_z that yields Fourier Transforms [39]. Therefore, the general solution for, say A_z , is given by

$$A_z = \int_{C_{k_\rho}} F(k_\rho) \Psi(k_\rho, k_z) dk_\rho \quad (29)$$

where C_{k_ρ} is the integration path in complex $k_\rho = \lambda + j\nu$ plane, [39,27,40]. $F(k_\rho)$ is a function that remains to be determined from the boundary conditions.

Consider the x -component of the magnetic vector potential in medium one, A_{x1} . Due to the radiation condition and the circular symmetry of the problem, constants $A_n = B_n = C_n = D_n = 0$ for $n \geq 1$; $A_0 = C_0 = 0, B_0 = D_0 = 1$, then

$$A_{x1} = \int_{k_\rho} F_x(k_\rho) H_0^{(2)}(k_\rho \rho) e^{-u_1 z} dk_\rho \quad (30)$$

where

$$u_1 = jk_{z1} = (k_\rho^2 - k_0^2)^{1/2} \quad (31)$$

and $k_0^2 = \omega^2 \epsilon_0 \mu_0$ is the wave number in free space. Similarly, for medium two [39]

$$A_{x2} = \int_{k_\rho} F_x(k_\rho) H_0^{(2)}(k_\rho \rho) \frac{\sinh u_2(z+h)}{\sinh(u_2 h)} dk_\rho \quad (32)$$

where

$$u_2 = jk_{z2} = (k_\rho^2 - \epsilon_r k_0^2)^{1/2}. \quad (33)$$

In the cylindrical coordinate system, the expression (13) for HED surface current distribution changes into

$$\mathbf{J}_s = \hat{\mathbf{x}} \frac{\delta(\rho)}{2\pi\rho} I dx. \quad (34)$$

Then function F_{k_ρ} is determined from the boundary condition on the normal derivative on A_x with the equation (34) substituted into (21)

$$\left(\frac{\partial A_{x2}}{\partial z} - \frac{\partial A_{x1}}{\partial z} \right)_{z=0} = \mu_0 \frac{\delta(\rho)}{2\pi\rho} I dx. \quad (35)$$

Taking the HED moment $I dx = 1$, the expressions for x -components of magnetic vector potential in media one and two are [39]

$$\begin{Bmatrix} A_{x1} \\ A_{x2} \end{Bmatrix} = \frac{\mu_0}{4\pi} \int_{k_\rho} H_0^{(2)}(k_\rho \rho) \frac{k_\rho}{D_{TE}} \begin{Bmatrix} e^{-u_1 z} \\ \frac{\sinh u_2(z+h)}{\sinh(u_2 h)} \end{Bmatrix} dk_\rho \quad (36)$$

with

$$D_{TE} = u_1 + u_2 \coth(u_2 h). \quad (37)$$

Boundary condition for z -directed component of magnetic vector potential at $z = 0$ is obtained from the relation (19), i.e., continuity of V across $z = 0$. This relation is written in terms of \mathbf{A} by applying the Lorentz gauge

$$\frac{1}{\epsilon_0} \frac{\partial A_{z1}}{\partial z} - \frac{1}{\epsilon_r \epsilon_0} \frac{\partial A_{z2}}{\partial z} = -\cos \phi \left(\frac{1}{\epsilon_0} - \frac{1}{\epsilon_r \epsilon_0} \right) \frac{\partial A_{x1}}{\partial \rho}. \quad (38)$$

This condition requires A_{z1}, A_{z2} to have $\cos \phi$ dependence. The final expression for z components of the magnetic vector potential \mathbf{A} is [39]

$$\begin{Bmatrix} A_{z1} \\ A_{z2} \end{Bmatrix} = -\frac{\mu_0}{4\pi} (\epsilon_r - 1) \cos \phi \times \int_{k_\rho} H_1^{(2)}(k_\rho \rho) \frac{k_\rho^2}{D_{TE} D_{TM}} \begin{Bmatrix} e^{-u_1 z} \\ \frac{\cosh u_2(z+h)}{\cosh(u_2 h)} \end{Bmatrix} dk_\rho \quad (39)$$

with

$$D_{TM} = \epsilon_r u_1 + u_2 \tanh(u_2 h). \quad (40)$$

Application of the Lorentz gauge (16) yields the expressions for scalar potentials V_1, V_2

$$\begin{Bmatrix} V_1 \\ V_2 \end{Bmatrix} = -\frac{\cos \phi}{4\pi j \omega \epsilon_0} \int_{k_\rho} H_1^{(2)}(k_\rho \rho) \frac{k_\rho^2 N}{D_{TE} D_{TM}} \begin{Bmatrix} e^{-u_1 z} \\ \frac{\sinh u_2(z+h)}{\sinh(u_2 h)} \end{Bmatrix} dk_\rho \quad (41)$$

with

$$N = u_1 + u_2 \tanh(u_2 h). \quad (42)$$

Note that A_z vanishes for the case of $\epsilon_r = 1$, and A_x is the same as for the case of HED above the ground plane. This completes the derivation of the potentials due to an x -directed HED. For the case of a y -directed HED, the derivation for potentials is the same, with y replacing x everywhere. Instead of ϕ we deal with $(\phi - \pi/2)$, therefore $\cos \phi$ is replaced by $\sin \phi$. (Any current on the $z = 0$ microstrip surface \mathbf{S}_p can be decomposed into its x - and y -directed components).

Once the potentials are known, the electric and magnetic fields are easily obtained by (14), (15).

2.3 Utilization of triangular basis functions

In order to solve for the surface current density, \mathbf{J}_s , the method of moments (MoM) [28] is applied. The triangular patches developed by Rao [30,31] are considered. The surface is triangulated, i.e., defined by an appropriate set of faces, edges, vertices and boundary edges. The salient features of triangular basis functions are summarized here [29]. Associated with each edge are two triangles defined by T_n^+ and T_n^- . The points on the triangle T_n^+ are defined by the position vector ρ_n^+ defined with respect to the free vertex of T_n^+ as shown in Figure 6. Similar remarks apply to the position vector ρ_n^- except that it is directed towards the free vertex of T_n^- . The plus or minus designation of the triangles are determined by the choice of a positive current reference direction for the n^{th} edge, which is assumed to be from T_n^+ to T_n^- . The vector basis functions, shown approximately in Figure 7, associated with the n^{th} edge are

$$\mathbf{f}_n(\mathbf{r}) = \begin{cases} \frac{\ell_n}{2A_n^+} \rho_n^+; & \mathbf{r} \text{ in } T_n^+ \\ \frac{\ell_n}{2A_n^-} \rho_n^-; & \mathbf{r} \text{ in } T_n^- \\ 0; & \text{otherwise} \end{cases} \quad (43)$$

where ℓ_n is the length of the edge, and A_n^\pm is the area of the triangle T_n^\pm . For this basis function, the current has no component normal to the boundary and hence no line charges exist along the boundary. The component of the current normal to the n^{th} edge is constant and continuous across the edge.

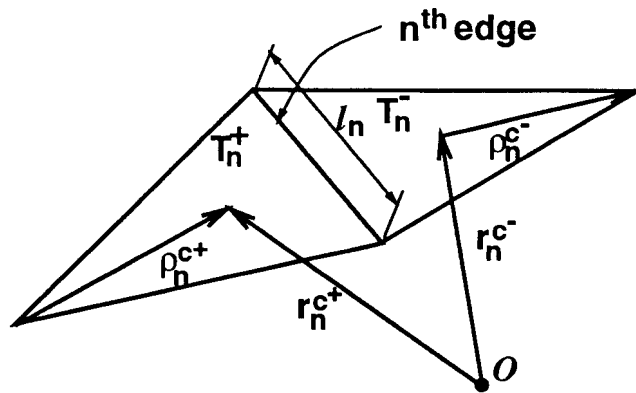


Figure 6. Global versus local coordinates associated with an edge in triangular patching.

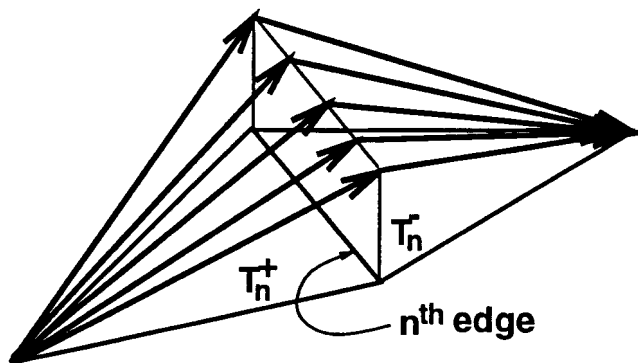


Figure 7. Vector basis function associated with an edge.

The surface divergence of the current basis function, which is proportional to the surface density associated with the basis element, is

$$\nabla_s \cdot \mathbf{f}_n(\mathbf{r}) = \begin{cases} \frac{\ell_n}{A_n^+}; & \mathbf{r} \text{ in } T_n^+ \\ \frac{\ell_n}{A_n^-}; & \mathbf{r} \text{ in } T_n^- \\ 0; & \text{otherwise} \end{cases} \quad (44)$$

The charge density is thus constant in each triangle, and the total charge associated with the triangle pair T_n^+ and T_n^- is zero.

The basis function \mathbf{f}_n is associated with each non-boundary edge of the triangulated structure. The current on the conducting patch is

approximated in terms of the \mathbf{f}_n as

$$\mathbf{J}_s \simeq \sum_{n=1}^N I_n \mathbf{f}_n(\mathbf{r}) = \sum_{n=1}^N I_n [\hat{x} f_{nx}(\mathbf{r}) + \hat{y} f_{ny}(\mathbf{r})] \quad (45)$$

where N is the number of nonboundary edges. In this expansion the functions f_{nx} and f_{ny} are the components of the basis functions in the x and y directions. Due to their association with each non-boundary edge, up to three non-zero basis functions may exist within each triangular face. At the edge, however, only the basis function associated with that edge has a component of current normal to the edge. Furthermore, since the normal component of \mathbf{f}_n at the n^{th} edge is unity, each coefficient I_n may be interpreted as the normal component of the current density flowing past the n^{th} edge.

To solve the integro-differential equation with the triangular basis functions, one has

$$L(\mathbf{J}_s)_{tan} = -\mathbf{E}_{tan}^i = 0 \quad (46)$$

$$\begin{aligned} L(\mathbf{J}_s)_{tan} = & \frac{j\omega\mu_0 I_n}{4\pi} \sum_{n=1}^N \left\{ \hat{x} \int_{T_n^\pm} f_{nx}(\mathbf{r}') \Pi_{xx} d\mathbf{r}' + \hat{y} \int_{T_n^\pm} f_{ny}(\mathbf{r}') \Pi_{yy} d\mathbf{r}' \right. \\ & \left. + \left[\hat{x} \frac{\partial}{\partial x} + \hat{y} \frac{\partial}{\partial y} \right] \cdot \int_{T_n^\pm} \nabla'_s \cdot \mathbf{f}(\mathbf{r}') \Pi_v d\mathbf{r}' \right\} \end{aligned} \quad (47)$$

where Π_{xx} , Π_{yy} , and Π_v are defined in the previous section and k_0 is the free space wave number.

The next step in applying the method of moments is to select the testing procedure. As testing functions, one chooses the same expansion functions \mathbf{f}_n for computational simplicity. The usual Hilbert inner product is used and since the weighting functions are real, it reduces to the conventional symmetric product. Therefore

$$V_m = \langle \mathbf{E}_{tan}^i, \mathbf{f}_m \rangle \simeq \ell_m \left[\mathbf{E}^i(\mathbf{r}_{m+}^c) \frac{\rho_{m+}^c}{2} + \mathbf{E}^i(\mathbf{r}_{m-}^c) \frac{\rho_{m-}^c}{2} \right] \quad (48)$$

where $\mathbf{r}_{m^\pm}^c$ is the vector from the origin to the centroid of the triangles T_m^\pm and $\rho_{m^\pm}^c$ is the vector from the free vertex to the centroid of the triangle T_m^\pm . The inner product is approximated over the triangles T_m^+ and T_m^- by the corresponding values of \mathbf{E}_{tan}^i at the centroids of the

triangle. A similar procedure is followed for $\langle L(\mathbf{J}), \mathbf{f}_m \rangle$ resulting in the matrix equation

$$[Z_{mn}][I_n] = [V_m] \quad (49)$$

An element of $[Z_{mn}]$ is then given by

$$\begin{aligned} [Z_{mn}] = \langle L(\mathbf{J}_n), \mathbf{f}_m \rangle &= \frac{j\omega\mu_0\ell_m}{4\pi} \sum_{m=m^+, m^-} \sum_{n=n^+, n^-} \\ &\left\{ \int_{T_n^\pm} \hat{x} f_{nx}(\mathbf{r}'_{n^\pm}) \Pi_{xx} \langle \mathbf{r}'_{n^\pm}, \mathbf{r}_{m^\pm}^c \rangle dr'_{n^\pm} + \int_{T_n^\pm} \hat{y} f_{ny}(\mathbf{r}'_{n^\pm}) \Pi_{yy} \langle \mathbf{r}'_{n^\pm}, \mathbf{r}_{m^\pm}^c \rangle dr'_{n^\pm} \right. \\ &\left. + \int_{T_n^\pm} \nabla'_s \cdot \mathbf{f}_n(\mathbf{r}'_{n^\pm}) \Pi_v \langle \mathbf{r}'_{n^\pm}, \mathbf{r}_{m^\pm}^c \rangle dr'_{n^\pm} \right\} \quad (50) \end{aligned}$$

The infinite integrals in the Hertzian potentials Π_{xx} , Π_{yy} , and Π_v are evaluated numerically by the procedure outlined in [39] and [27].

Each element of $[Z_{mn}]$ consists of four terms. The superscripts of $+$ and $-$ on m and n represent the two triangles associated with both the expansion and the testing triangle functions, m and n respectively. Therefore the integration has to be performed carefully on the proper triangle. So each element of $[Z_{mn}]$ is associated with the pair of nonboundary edges m and n . However, the domains of the integrals and locations of the observation points are associated with the faces attached to these edges.

Once $[Z_{mn}]$ and $[V_m]$ are known, the current amplitudes $[I_n]$ are easily obtained by solving complex matrix equation (49) by Gaussian elimination. However, before solving for current distribution, in order to find S- parameters of the circuit, we modify the MoM matrix by enforcing a match-terminating condition on transmission line currents, as presented in the next section.

2.4 Numerical simulation of a match-termination

Microwave circuits are usually described by scattering parameters, defined here for a two-port network

$$\begin{aligned} \mathbf{b}_1 &= S_{11} \mathbf{a}_1 + S_{12} \mathbf{a}_2 \\ \mathbf{b}_2 &= S_{21} \mathbf{a}_1 + S_{22} \mathbf{a}_2 \end{aligned} \quad (51)$$

where $\mathbf{a}_k = \mathbf{I}_k^+ \sqrt{Z_0}$ and $\mathbf{b}_k = -\mathbf{I}_k^- \sqrt{Z_0}$, $k = 1, 2$, are incident and reflected waves, respectively, and $\mathbf{I}_k = \mathbf{I}_k^+ + \mathbf{I}_k^-$.

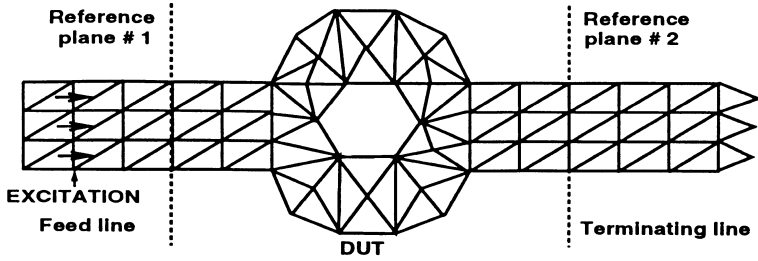


Figure 8. A two-port, microstrip device-under-test (DUT), inserted between a feed line and a terminating line. Triangular patching is also shown.

The simplest way to determine S_{11} and S_{21} is to match-terminate port # 2, i.e., to make $\mathbf{a}_2 = 0$, and to apply the excitation \mathbf{a}_1 at port # 1, as shown in Figure 8, the end result being

$$S_{11} = \frac{\mathbf{b}_1}{\mathbf{a}_1} \quad \& \quad S_{21} = \frac{\mathbf{b}_2}{\mathbf{a}_1} \quad (52)$$

The parameters S_{22} and S_{12} are obtained similarly by exciting port # 2 and match-terminating port # 1. This procedure is also used in vector network measurements. Our goal is to incorporate the same procedure in our numerical analysis.

The current $I(x)$ along a lossless, 2-directed transmission line is given by

$$I(x) = I_0^+ e^{-j\beta x} + I_0^- e^{+j\beta x} \quad (53)$$

as a sum of a forward traveling and a backward traveling current wave. On a match-terminated line, there is no reflection from the load, therefore

$$I(x) = I_0^+ e^{-j\beta x} \quad (54)$$

where

$$\beta = \frac{2\pi}{\lambda_g} = \frac{2\pi f \sqrt{\epsilon_{reff}}}{c_0},$$

f being the frequency, c_0 speed of light in the free space, and $\epsilon_{r_{eff}}$ effective dielectric constant of the microstrip. We find the $\epsilon_{r_{eff}}$ from a frequency-dependent empirical formula given in [41].

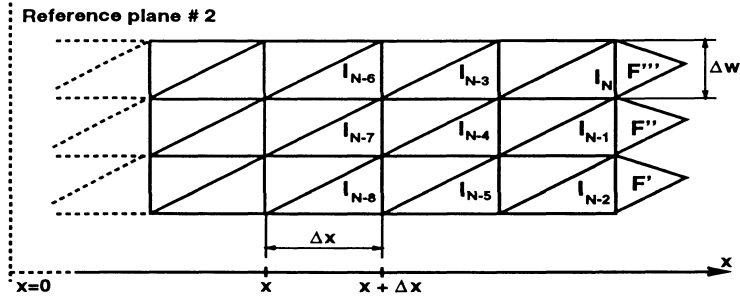


Figure 9. Terminating line at port # 2. Three sections across the line width are used.

If the reference is shifted from zero to a point x on the line, then complex current at the point: $x + \Delta x$, shown in Figure 9, becomes

$$I(x + \Delta x) = I_x e^{-j\beta\Delta x} \quad (55)$$

Quantities $I_k, k = N, N - 3, N - 6, \dots$ stand for currents across vertical internal edges that are located Δx apart, for the case of terminating line in Figure 9 with three sections across. The condition (55) then becomes

$$-e^{-j\beta\Delta x} I_{k-3} + I_k = 0, \quad k = N, N - 1, N - 2, \dots, N - I_{term} \quad (56)$$

where I_{term} determines how far from the end of the line the match-terminating condition is to be enforced (typically $10 \cdot h$ away from the end, h being the substrate thickness).

These relations (56) are in addition to the N equations (49), for a total of $(N + I_{term})$ equations with N unknowns. This yields an over-determined linear system of equations that can be handled by a least-squares approach. However, we chose to eliminate I_{term} rows of the original MoM equation (49) and replace them with I_{term} match-terminating conditions (55), resulting in an $N \times N$ linear system. This newly obtained linear system, i.e., matrix equation, has I_{term} rows with only two non-zero elements. We show the N^{th} one here

$$\begin{bmatrix}
Z_{11} & \dots & Z_{1N-3} & Z_{1N-2} & Z_{1N-1} & Z_{1N} \\
Z_{21} & \dots & Z_{2N-3} & Z_{2N-2} & Z_{2N-1} & Z_{2N} \\
\vdots & & & & & \\
Z_{k1} & \dots & Z_{kN-3} & Z_{kN-2} & Z_{kN-1} & Z_{kN} \\
\vdots & & & & & \\
Z_{N11} & \dots & Z_{N-1N-3} & Z_{N-1N-2} & Z_{N-1N-1} & Z_{N-1N} \\
0 & \dots & -e^{-j\beta\Delta x} & 0 & 0 & 1
\end{bmatrix}
\begin{bmatrix}
I_1 \\
I_2 \\
\vdots \\
I_k \\
\vdots \\
I_{N-1} \\
I_N
\end{bmatrix}
=
\begin{bmatrix}
V_1 \\
V_2 \\
\vdots \\
V_k \\
\vdots \\
V_{N-1} \\
0
\end{bmatrix}
\quad (57)$$

In order to eliminate these zeroes and reduce the size of the modified MoM matrix, we replace the variable I_N with $e^{-j\beta\Delta x}I_{N-3}$, which results in

$$\begin{bmatrix}
Z_{11} & \dots & Z_{1N-3} + e^{-j\beta\Delta x}Z_{1N} & Z_{1N-2} & Z_{1N-1} \\
Z_{21} & \dots & Z_{2N-3} + e^{-j\beta\Delta x}Z_{2N} & Z_{2N-2} & Z_{2N-1} \\
\vdots & & & & \\
Z_{k1} & \dots & Z_{kN-3} + e^{-j\beta\Delta x}Z_{kN} & Z_{kN-2} & Z_{kN-1} \\
\vdots & & & & \\
Z_{N11} & \dots & Z_{N-1N-3} + e^{-j\beta\Delta x}Z_{N-1N} & Z_{N-1N-2} & Z_{N-1N-1}
\end{bmatrix}
\begin{bmatrix}
I_1 \\
I_2 \\
\vdots \\
I_k \\
\vdots \\
I_{N-1}
\end{bmatrix}
=
\begin{bmatrix}
V_1 \\
V_2 \\
\vdots \\
V_k \\
\vdots \\
V_{N-1}
\end{bmatrix}
\quad (58)$$

This procedure is repeated I_{term} times, yielding an $(N - I_{term})$ by $(N - I_{term})$ linear system. We use Gaussian elimination to solve this system for the unknown current coefficients.

Triangle faces F' , F'' , F''' , shown in Figure 9 are added to the end of the terminating line in order to make boundary edges n , $n-1$ and $n-2$ into internal edges. However, we do not take faces F' , F'' , F''' into account when evaluating elements of the Z matrix, the end result being that unknown charges accumulate on these triangles. A simple physical explanation of our match-termination is that the forward-traveling current wave on the terminating line carries all the charges onto the faces F' , F'' , F''' , where the charge distribution is singular. This, however, has no effect on the current distribution in the device-under-test region; as an observer located in the reference plane # 2, (Figure 9), sees no reflection from the end of the terminating line, therefore the terminating line appears to be matched.

Once the current distribution on the microstrip structure is solved for, we employ the “Matrix Pencil” method to decompose currents on the feed line into forward and backward traveling waves, I_1^+ and I_1^- . Similarly, the forward traveling wave I_2^+ on the terminating line is determined. Then, in accordance with (52)

$$S_{11} = -\frac{I_1^-}{I_1^+} \quad \& \quad S_{21} = \frac{I_2^+}{I_1^+} \quad (59)$$

Parameters S_{12} and S_{22} are determined in a similar fashion, by exciting the port # 2 and match-terminating the port # 1.

Knowing the current distribution on the microstrip, we easily obtain the far-field radiation pattern, as presented in [39,29]. This feature is of the greatest importance for the case of microstrip patch antennas.

This whole procedure is done for characterization of the structure at one single frequency only. We have implemented a computer code that sweeps over a desired range of frequencies, and gives current and voltage distributions on the structure, S-parameters and the far-field pattern.

The Matrix Pencil approach is outlined in the next section.

3. Matrix Pencil

In the matrix pencil [32], the objective is to fit a complex function by a sum of complex exponentials

$$\mathbf{I}(x) \cong \sum_{i=1}^M A_i e^{\gamma_i x}, \quad (60)$$

where γ_i are the complex exponents and A_i are complex amplitudes. Here M (the number of complex exponentials) is unknown and so are the complex propagation constants γ_i and the amplitudes A_i of the various components. One of the objectives of using the matrix pencil approach is to also solve for M .

The method has been described in detail in [32] and [33], and has been demonstrated to be very robust to statistical noise [33].

The complex function that we are interested in decomposing is the current along the microstrip transmission line. Complex exponentials then acquire a physical meaning, for they are propagating modes — forward and backward dominant modes, and higher order modes (complex or leaky waves) along the transmission line. Our numerical method, described in the previous section, solves for the current distribution on the microstrip structure, from which the current along the feed or terminating transmission line is easily determined. Let us label these equidistant currents across the line by $y_0, y_1, \dots, y_k, \dots, y_{n-1}, y_n$, starting from the reference plane, as shown in Figure 10.

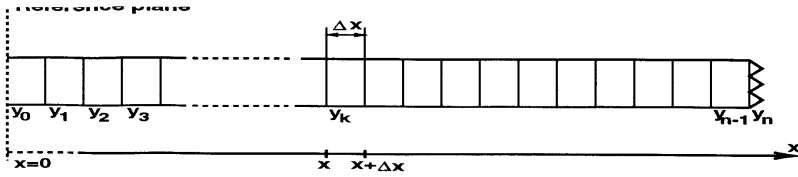


Figure 10. Current distribution along the feed/terminating microstrip line.

Following generalized pencil-of-function (GPOF) method [32], we define matrices Y_1 and Y_2 as

$$Y_1 = \begin{bmatrix} y_0 & y_1 & \cdots & y_{L-2} & y_{L-1} \\ y_1 & y_2 & \cdots & y_{L-1} & y_L \\ \vdots & & & & \\ y_{N-L-1} & y_{N-L} & \cdots & y_{N-3} & y_{N-2} \end{bmatrix}, \quad (61)$$

and

$$Y_2 = \begin{bmatrix} y_1 & y_2 & \cdots & y_{L-1} & y_L \\ y_2 & y_3 & \cdots & y_L & y_{L+1} \\ \vdots & & & & \\ y_{N-L} & y_{N-L+1} & \cdots & y_{N-2} & y_{N-1} \end{bmatrix}, \quad (62)$$

provided $N, L \leq n$.

Then we create matrix pencil $Y_2 - zY_1$ that can be represented as a generalized eigenvalue problem

$$Y_2 - zY_1 = Z_1 A (Z_0 - I\lambda) Z_2 \quad (63)$$

Namely, when $M \leq L \leq N - M$ then the poles $z_i = e^{\gamma_i \Delta x}, i = 1, \dots, M$ are the generalized eigenvalues of the matrix pencil $Y_2 - zY_1$. Also, the rank of matrix pencil is equal to the number of signal poles M , unless $z = z_i$. Generalized eigenvalues of the matrix pencil, i.e., signal poles, are obtained by using singular value decomposition (SVD) algorithm.

Complex magnitudes, $A_i, i = 1, \dots, M$ are solved by least squares from

$$\begin{bmatrix} y_0 \\ y_1 \\ \vdots \\ y_{N-1} \end{bmatrix} = \begin{bmatrix} 1 & 1 & \dots & 1 \\ z_1 & z_2 & \dots & z_M \\ \vdots & \vdots & \ddots & \vdots \\ z_1^{N-1} & z_2^{N-1} & \dots & z_M^{N-1} \end{bmatrix} \begin{bmatrix} A_1 \\ A_2 \\ \vdots \\ A_M \end{bmatrix} \quad (64)$$

If the number of poles, M , is not known, it can be estimated from the singular values

$$\sigma_1 \geq \sigma_2 \geq \dots \geq \sigma_M \geq \dots \geq \sigma_{\min(N-L, L)} \quad (65)$$

since $\sigma_{M+1} = \dots = \sigma_{\min(N-L, L)} = 0$ for noiseless data. In case of noisy data y_k , the largest M singular values of $Y_1, \sigma_1, \dots, \sigma_M$ should be chosen.

4. Menzel's leaky-wave antenna

In his 1979 paper [35], Menzel presented a new traveling-wave antenna in microstrip, fed in its first higher order mode and operated near the cutoff frequency of that mode. He approximated the edges of radiating patches by slot antennas and neglected dielectric-air boundary. (The exact characterization of the microstrip had not been done at that time.) He assumed the existence of the first higher order mode on the microstrip with a real propagating constant. However, in 1976, Ermert [42] showed that such a mode could not exist in the given frequency range. The main significance of his antenna was a high gain

for its short physical length — only $2.23 \lambda_0$. He obtained favorable agreement between his and experimental results; however, he failed to explain why this “traveling-wave” antenna radiated so well with its short length, and why propagation constant of the first higher mode is real.

In a technical report [37] and in his 1987 paper [36], Oliner shows that the first higher order mode has complex propagation wavenumber (leaky mode) and that this “traveling-wave” antenna is actually a leaky-wave antenna, therefore resolving the contradiction between [35] and [42]. We analyze the Menzel’s antenna by our numerical method and compare it with Oliner’s theoretical and Menzel’s experimental results.

The geometry of Menzel’s antenna is shown in Figure 11. It is a 100 mm long, 15 mm wide section of open-ended microstrip line, on $h = 0.794$, $\epsilon_r = 2.32$ dielectric substrate, fed unsymmetrically with a 50Ω , 2.3 mm wide line. We triangularize the structure and solve for the current distribution on it. We consider 10 sections across, 60 sections along the antenna, and two sections across, 50 sections along the feed line. Figure 12 shows the comparison between our results (solid line for $\epsilon_r = 2.42$, circles for $\epsilon_r = 2.32$) and experimental results from Menzel’s paper [35] (dashed line) at an operating frequency of 6.7 GHz. Our result, obtained for $\epsilon_r = 2.42$, coincides with the experimental one, supposedly measured for substrate of $\epsilon_r = 2.32$. The value for ϵ_r of 2.42 is only 4.3% away from prescribed $\epsilon_r = 2.32$, therefore within the 5% tolerance range for the dielectric constant.

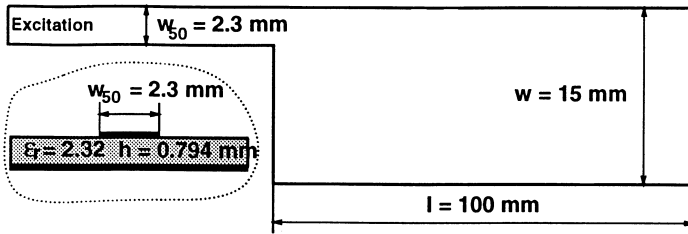


Figure 11. Geometry of Menzel’s antenna.

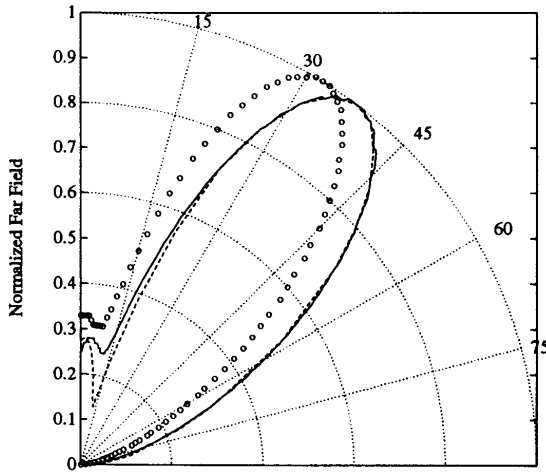


Figure 12. Normalized far field pattern of Menzel's antenna at 6.7 GHz: Menzel's experimental result (dashed line) versus our results for $\epsilon_r = 2.42$ (solid line) and for $\epsilon_r = 2.32$ (o o o).

Furthermore, Oliner [37,36], shows that the current along the Menzel's antenna at frequency of 6.7 GHz can be described by a single complex mode. The normalized real (β/k_0) and imaginary part (α/k_0) of the propagation wavenumber are given in Table 1, alongside the Menzel's and our results. Menzel assumed a real propagation constant, therefore his $\alpha/k_0 = 0$. Oliner arrives at his value for complex propagation wavenumber through a rigorous Wiener-Hopf approach [43] and steepest-descent analysis [37]. We obtain our values for propagation wavenumber by decomposing current along one edge of the antenna into complex exponentials by our Matrix Pencil method. Menzel's, Oliner's and our value for β/k_0 are within 2.5% from each other, while our value for α/k_0 is of the same order as Oliner's. The relatively large value of α/k_0 ($= 0.05$) explains why Menzel's antenna radiates so well despite its short length ($2.23 \lambda_0$), approximately 65% of incoming power is actually radiated. Leaky-wave antennas are typically designed to radiate at least 90% of the power. Menzel's antenna would do so if its length is increased from 100 mm ($2.23 \lambda_0$) to 217 mm ($4.85 \lambda_0$). The main beam-width then reduces from 26° to more practical 14° [37,36].

	β/k_0	α/k_0
Menzel	0.645	0.00
Oliner	0.661	0.04
Our work	0.647	0.05

Table 1. Normalized real (β/k_0) and imaginary (α/k_0) of the propagation wavenumber for the first higher order mode on Menzel’s antenna.

Another useful property of this antenna is that the position of its main beam can be swept by a change of the operating frequency, as demonstrated in Figure 13. Oliner’s results [37] for the normalized far field pattern of a 217 mm long version of Menzel’s antenna is shown for frequencies of 6.7 GHz (o o o), 7.5 GHz (x x x) and 8.5 GHz (+ + +) in comparison with results obtained by our method (solid line). Oliner uses ϵ_r of 2.32, but we consider $\epsilon_r = 2.42$. The agreement between Oliner’s and our results is excellent for frequencies of 7.5 GHz and 8.0 GHz, and very good for $f = 6.7$ GHz. If we consider $\epsilon_r = 2.32$, then the far field pattern for all three frequencies rotates for approximately 8° counterclockwise, with no other changes.

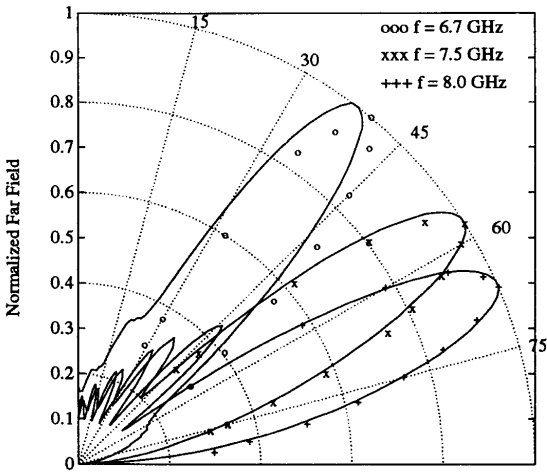


Figure 13. Normalized far field pattern of of 217 mm long Menzel’s antenna at 6.7 GHz, 7.5 GHz, and 8.0 GHz. Oliner’s results for frequencies of 6.7 GHz (o o o), 7.5 GHz (x x x) and 8.5 GHz (+ + +) are compared with results obtained by our method (solid line). Oliner uses $\epsilon_r = 2.32$, while we consider $\epsilon_r = 2.42$.

5. Experimental verification

In this section we compare our numerical results with experiments, and, when available, analysis by “Super-Compact”, a commercial software package. We obtain experimental results on the HP 8510B vector network analyzer using a microstrip test fixture as sketched in Figure 14. The HP 8510B is calibrated using a set of precise coaxial standards for short, open, matched load and sliding load, in the full two-port procedure. The calibration effectively establishes the analyzer’s measurement reference planes at the ends of the test cables. If we measure scattering (S) parameters of our microstrip device mounted on the test fixture, we obtain characteristics of microstrip device embedded between connectors A and B (Figure 15). It is our goal to extract

$$\mathbf{S}_{\text{DUT}} = \begin{bmatrix} S_{11} & S_{12} \\ S_{21} & S_{22} \end{bmatrix} \quad (66)$$

the scattering parameters matrix of the device under test (DUT) only. In order to do so, we perform a de-embedding procedure, in which the effects of the connectors are determined and accounted for.

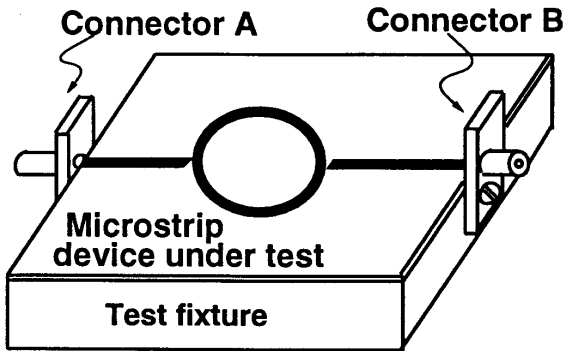


Figure 14. A microstrip test fixture.

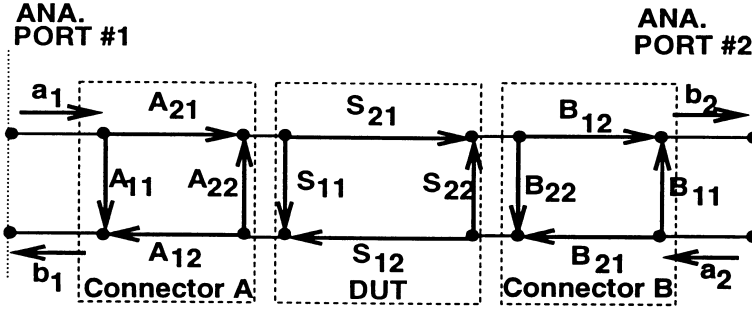


Figure 15. Signal flow-chart of the test fixture with microstrip device under test.

5.1 Microstrip device under test de-embedding

Our approach is based on a broad-band device de-embedding method using the automatic network analyzer time-domain option as described by Gronau and Wolff [44, 45]. The signal flow chart of the (DUT) is characterized by S_{11} , S_{21} , S_{12} , and S_{22} . Parameters A_{ij} , B_{ij} , $i, j = 1, 2$, represent connectors A and B respectively (Figure 15). To assemble our test fixture, we use “M/A COM Omni Spectra” coaxial connectors, serial number 2052-5416-00. The connectors cost less than \$30.00 each — very affordable if compared to “Inter-Continental Microwave” microstrip test fixture that costs \$5,000.00 and does not provide as good of a connection for our purposes, at least with devices manufactured on $\epsilon_r = 2.33$, $h = 0.508$ mm dielectric substrate. Connectors are reciprocal passive devices, therefore $A_{21} = A_{12} = A$ and $B_{21} = B_{12} = B$. Based on identical physical (and electrical) length of connectors A and B, we make another simplifying assumption, $A = B$. Furthermore, from the physical characteristics of the “M/A COM Omni Spectra” connectors, namely physical length $l_{conn} \approx 9.75$ mm and dielectric core $\epsilon_{r_{conn}} = 2.25$ (polyethylene), it follows that

$$\varphi_A = \angle A \approx e^{-j2\pi f \frac{1}{c_0} \sqrt{\epsilon_{r_{conn}}} l_{conn}}, \quad (67)$$

where f is the operating frequency and c_0 is the speed of light in free space.

In order to determine $|A|$, A_{11} , A_{22} , B_{11} and B_{22} , a simple device of known characteristics is inserted in the test fixture and measured.

We use a section of microstrip transmission line of known length l_1 (Figure 16).

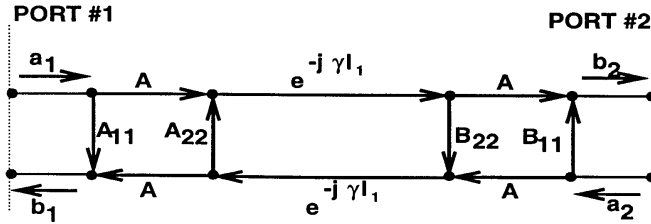


Figure 16. Signal flow-chart of the test fixture with a transmission line of length l_1 .

Using the impulse band-pass time-domain option on the HP 8510B, we obtain the reflection time-domain response on test port # 1 of the test fixture with a line of length l_1 as shown in Figure 17. Reflections from connectors A and B are clearly separated in time. (The test line has to be long enough so that there is no interaction between connectors in the time-domain). On the HP 8510B, the time-domain response of the DUT is obtained by applying an inverse Fourier transform to the frequency-domain measurements [46]. The time-domain resolution is directly proportional to the measurement frequency span ($f_{stop} - f_{start}$). A wider frequency span provides for better resolution in time-domain. Here, we chose the frequency range to be 0.1 - 20.1 GHz. A choice of $l_1 = 101.6$ mm proves to be sufficiently long.

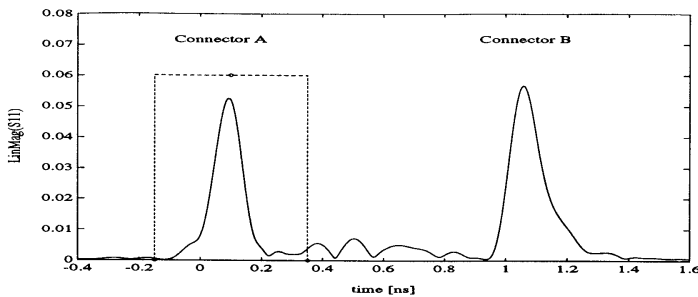


Figure 17. Impulse time-domain response of a 4-inch microstrip line with connectors; $\epsilon_r = 2.33$, substrate thickness $h=0.508$ mm, $Z_0 = 50\Omega$.

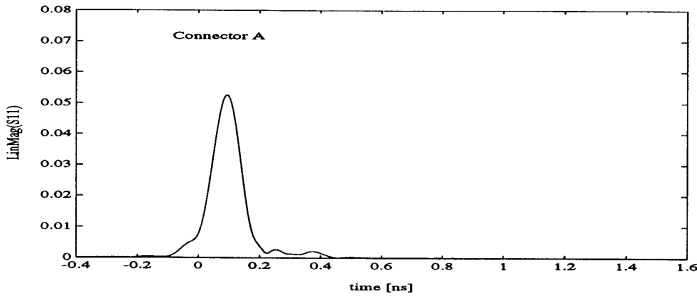


Figure 18. Gated impulse time-domain response of a 4-inch microstrip line with connectors; reflection from the connector B removed.

In the time-domain response, it is possible to remove the effects of unwanted mismatches, or to isolate the response of an individual mismatch, by using the gating feature. Figure 18 shows the isolated response of the connector A only, obtained by application of a “gate” centered on connector A response, with a span of 500 ps. For a given measurement frequency span, there is a prescribed minimum gate span that has to be used in order to get meaningful results [46]. For a “wide” gate shape, minimum gate span equals $8.0/f_{span} = 400$ ps given $f_{span} = 20$ GHz. However, there is also an upper limit on the gate span - in order to be able to effectively separate effects of individual connector, it has to be smaller than the time distance between connectors A and B. A gate span of 500 ps satisfies both of these conditions. The gated time-domain response of the connector A is then transformed back to the frequency-domain, yielding A_{11} directly. Figure 19 shows comparison of S_{11} response of the test fixture with 101.6 mm long line, and S_{11} response from connector A only. Similar procedure yields B_{11} , by centering the gate on connector B in S_{22} time-domain response.

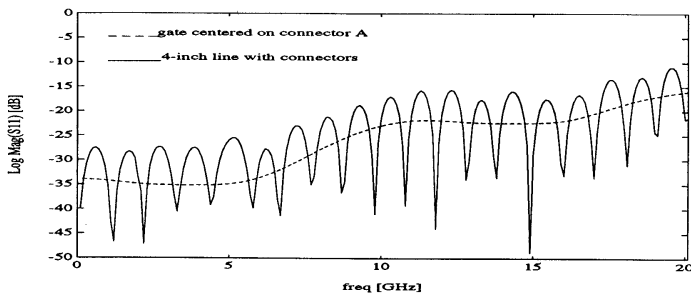


Figure 19. Parameters S_{11} of the test fixture with a line of length $l_1=101.6$ mm compared to S_{11} of the connector A.

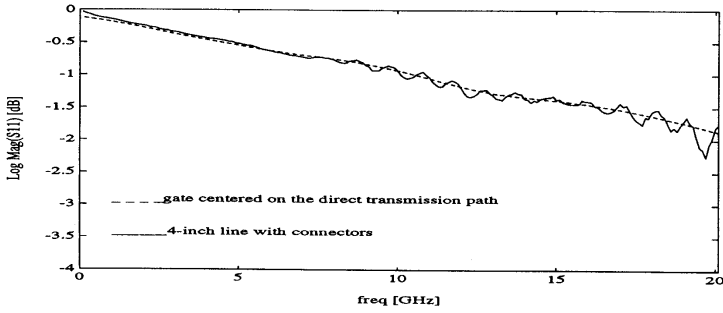


Figure 20. Parameter S_{21} of the test fixture with a line of length $l_1=101.6$ mm compared to gated direct-path of S_{21} .

Next, the gate is placed on connector B in S_{11} time-domain response. A Fourier transform back to frequency domain yields

$$C_1 = A^2 B_{22} e^{-2\gamma l_1} \quad (68)$$

where $\gamma = \alpha + j\beta$ is the complex propagation constant for the quasi-TEM mode on microstrip line.

In a similar fashion, gating connector A in the S_{22} response produces

$$C_2 = A^2 A_{22} e^{-2\gamma l_1} \quad (69)$$

The transmission coefficient, S_{21}^M , from port # 1 to port # 2 is related to the connector and line parameters by

$$S_{21}^M = \frac{A^2 e^{-\gamma l_1}}{1 - A_{22} B_{22} e^{-2\gamma l_1}}. \quad (70)$$

The denominator of the above expression is removed by setting the gate on the direct path in time-domain response of S_{21}^M and transforming it back to the frequency domain as shown in Figure 20. When applied to the transmission measurement, the gating procedure removes the response of the multiple transmission paths between connectors A and B. The resulting equation is

$$C_3 = A^2 e^{-\gamma l_1}. \quad (71)$$

So far, coefficients A_{11} , B_{11} and $\angle A$ were obtained directly. The remaining unknowns are A_{22} , B_{22} , $|A|$, and γ . Therefore, at least one

more standard is needed: we choose another section of transmission line of length $l_2 = l_1/2$. Gating the direct path in S_{21}^M yields

$$C_4 = A^2 e^{-\gamma l_2} = A^2 e^{-\frac{1}{2}\gamma l_1}. \quad (72)$$

Let

$$K_1 = e^{-\gamma l_1} \quad (73)$$

Then, from (71), (72)

$$K_1 = \left(\frac{C_3}{C_4} \right)^{\frac{1}{2}} \quad (74)$$

$$A = \sqrt{\left| \frac{C_3}{K_1} \right|} e^{j\varphi_A} \quad (75)$$

Substitution of A into equations (68) and (69) yields

$$A_{22} = \frac{C_2}{A^2 K_1^2} \quad (76)$$

$$B_{22} = \frac{C_1}{A^2 K_1^2}. \quad (77)$$

The scattering matrices \mathbf{S}_A and \mathbf{S}_B representing connectors A and B are defined by

$$\mathbf{S}_A = \begin{bmatrix} A_{11} & A \\ A & A_{22} \end{bmatrix} \quad \text{and} \quad \mathbf{S}_B = \begin{bmatrix} B_{22} & A \\ A & B_{11} \end{bmatrix}. \quad (78)$$

Since connector A, the DUT, and connector B are in a cascade, it is convenient to transform the S parameters to the wave-transmission (T) parameters, by using transform

$$\mathbf{T} = \begin{bmatrix} \frac{1}{S_{21}} & -\frac{S_{22}}{S_{21}} \\ \frac{S_{11}}{S_{21}} & \frac{S_{12}S_{21} - S_{11}S_{22}}{S_{21}} \end{bmatrix} \quad \text{and} \quad \mathbf{S} = \begin{bmatrix} \frac{T_{21}}{T_{11}} & \frac{T_{11}T_{22} - T_{21}T_{12}}{T_{11}} \\ \frac{1}{T_{11}} & -\frac{T_{12}}{T_{11}} \end{bmatrix}. \quad (79)$$

Let \mathbf{T}_{DUT} corresponds to \mathbf{S}_{DUT} , \mathbf{T}_A to \mathbf{S}_A and \mathbf{T}_B to \mathbf{S}_B . Since

$$\mathbf{T} = \mathbf{T}_A \mathbf{T}_{\text{DUT}} \mathbf{T}_B, \implies \mathbf{T}_{\text{DUT}} = \mathbf{T}_A^{-1} \mathbf{T} \mathbf{T}_B^{-1}. \quad (80)$$

Finally, \mathbf{T}_{DUT} yields \mathbf{S}_{DUT} , the scattering parameters of the de-embedded device under test. Figure 21 shows the difference between

“raw” measured and de-embedded reflection characteristics of our 4-inch section of microstrip transmission line.

Figure 21 also shows that the de-embedding reduces reflection measurement error by approximately 20 dB, or by an order of magnitude across the frequency span. This improvement is particularly significant in reflection measurements of low-reflection devices. The residual error is primarily due to less-than-excellent repeatability of connector to microstrip line connections. Also, this de-embedding procedure assumes a good isolation between connectors, an assumption that is not always true.

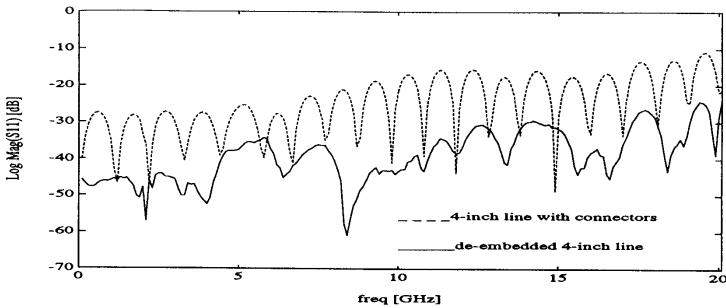


Figure 21. Magnitude of S_{11} (logarithmic scale) of $l=101.6$ mm line with connectors, compared to de-embedded line.

5.2 Interdigital capacitor

An interdigital capacitor is treated here as a series two-port element. Its dimensions are shown in Figure 22. since Super-Compact does not have capability to analyze this particular capacitor, Figures 23 – 26 show the comparison between our numerical results and measurements only. These compare favorably, in particular for the resonant behavior at frequency $f = 6.1$ GHz.

This type of capacitor is used in microwave integrated circuits to realize small capacitances, provided that its overall dimensions are much smaller than the wavelength λ_g . In order to determine the applicable frequency range for this device, we shift S-parameters reference planes 8 mm towards the capacitor, in order to “zoom” in on it. The computed parameter S'_{11} is shown in Figure 27 in the Smith-chart format. Since the bottom-half of the impedance Smith-chart is capacitive,

it follows that this capacitor acts as an inductor beyond $f \approx 5.65$ GHz! To find an approximate value of equivalent capacitance C , the imaginary part of input impedance is obtained from S_{11} , i.e.,

$$\Im\{Z_{in}\} \approx \frac{-j}{2\pi f C} = \Im\left\{Z_0 \frac{1 + S_{11}}{1 - S_{11}}\right\}.$$

At frequency $f = 1.6$ GHz, $Z_{in} = (2.2 - j100)\Omega$, yielding $C = 1/2\pi f \Im\{Z_{in}\} \approx 1$ pF. Similarly, at $f = 3$ GHz, $C \approx 1.3$ pF. The resonance at $f = 6.1$ GHz occurs when the capacitor acts as a bank of quarter-wavelength ($\lambda_g/4$) couplers. Indeed, at $f = 6.1$ GHz, the wavelength on the microstrip line $\lambda_g = \lambda_0/\sqrt{\epsilon_{reff}} \approx 36$ mm. The total length of the capacitor is approximately 9mm, which is exactly $\lambda_g/4$ at $f = 6.1$ GHz. Therefore, this capacitor has practical use in the frequency range up to $f \approx 2.5$ GHz only.

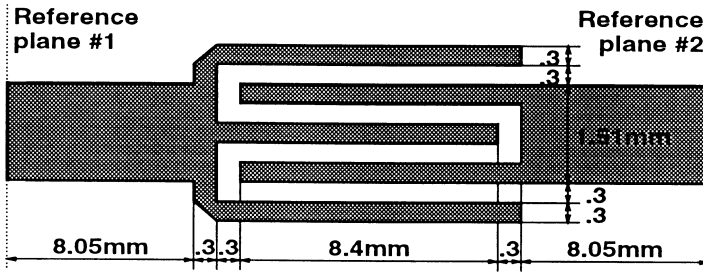


Figure 22. Series interdigital capacitor; all dimensions in millimeters.

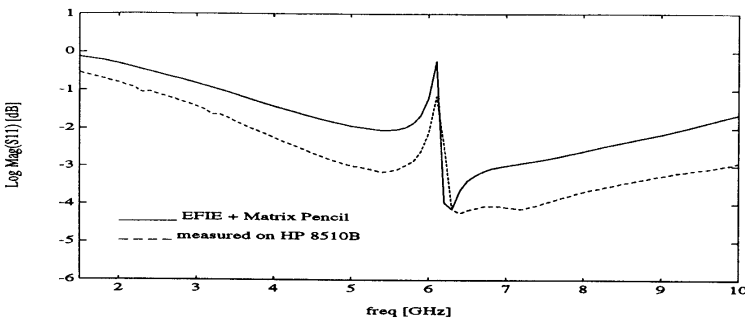


Figure 23. Magnitude of S_{11} of series interdigital capacitor.

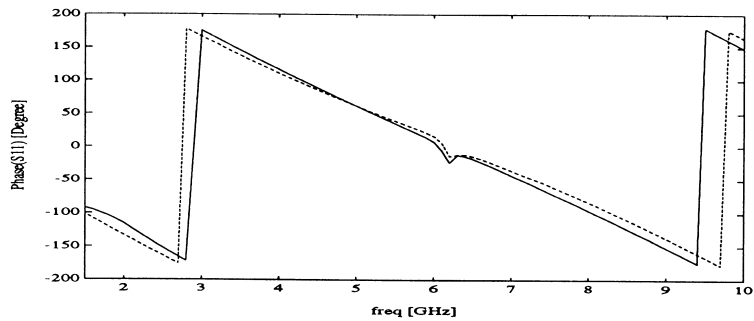


Figure 24. Phase of S_{11} of series interdigital capacitor.

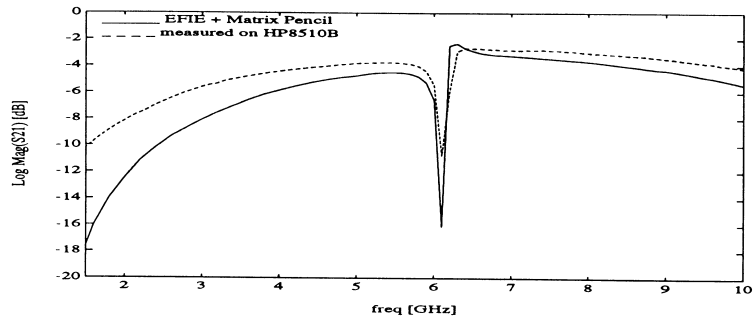


Figure 25. Magnitude of S_{21} of series interdigital capacitor.

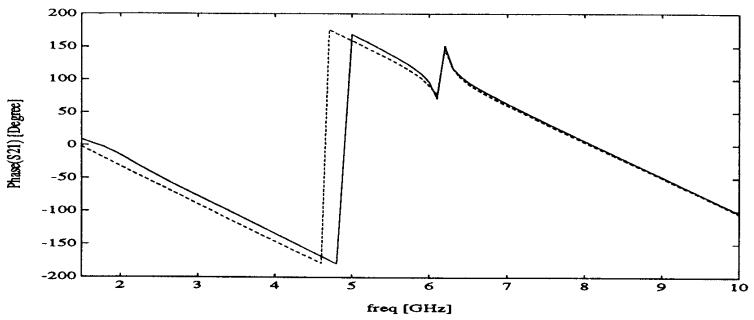


Figure 26. Phase of S_{21} of series interdigital capacitor.

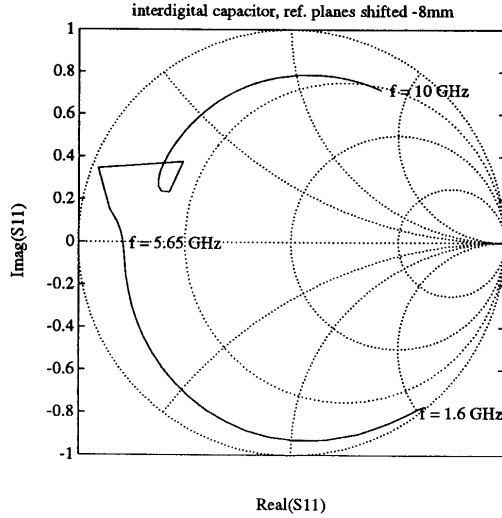


Figure 27. S_{11} of series interdigital capacitor; reference planes shifted inwards by 8 mm.

5.3 Single loop inductor

Figure 28 shows layout of a single-loop inductor, its scattering parameters are presented in Figures 29–32. The solid-line trace represents our numerical results, the dashed-line represents data measured on the HP 8510B. Overall, there is a favorable agreement between numerical and experimental results. Super-Compact does not have a model for this device. Again, as in the case of a capacitor, this inductor can be used in microwave integrated circuits, provided that its overall dimensions are much smaller than wavelength λ_g . Figure 33 shows the computed scattering parameter S'_{11} in Smith-chart format, reference planes being shifted 10 mm towards the inductor. (This reference plane shift is introduced in order to capture characteristics of the inductive loop only). The inductor behaves as an inductor up to $f \approx 2$ GHz, while it is predominantly capacitive in the 2 – 4.4 GHz frequency range. At $f \approx 4.4$ GHz, the capacitive effect is canceled by the inductive effect, which explains the resonant behavior at this frequency in Figure 30. From

$$L = \frac{\Im\{Z_{in}\}}{2\pi f},$$

it follows that $L \approx 9.6$ nH, at $f = 1.5$ GHz. The physical length of the inductive loop is ≈ 24 mm, which corresponds to $\approx \lambda_0/8$ at $f = 1.5$ GHz. Hence, this device should not be intended for use as an inductor beyond a frequency of 1.5 GHz.

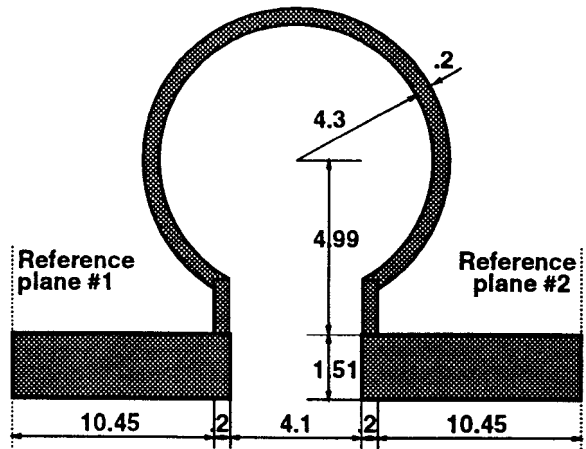


Figure 28. Single loop inductor; all dimensions in millimeters.

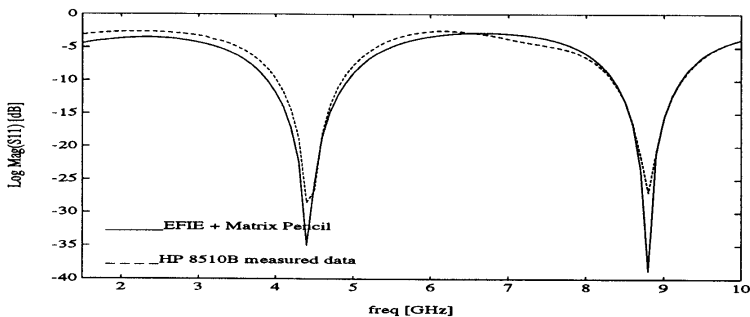


Figure 29. Magnitude of S_{11} of series single loop inductor.

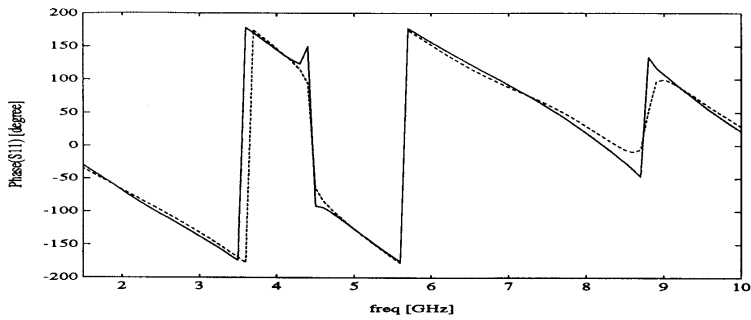


Figure 30. Phase of S_{11} of series single loop inductor.

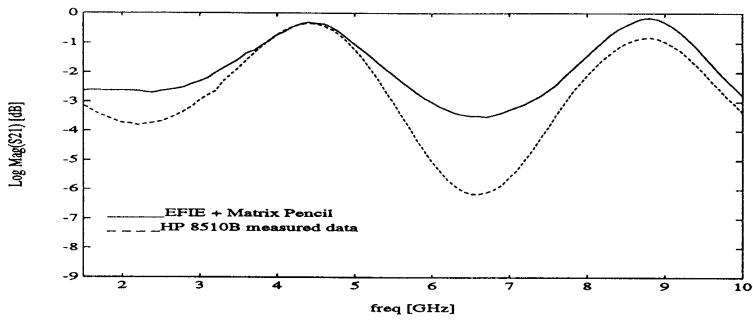


Figure 31. Magnitude of S_{21} of series single loop inductor.

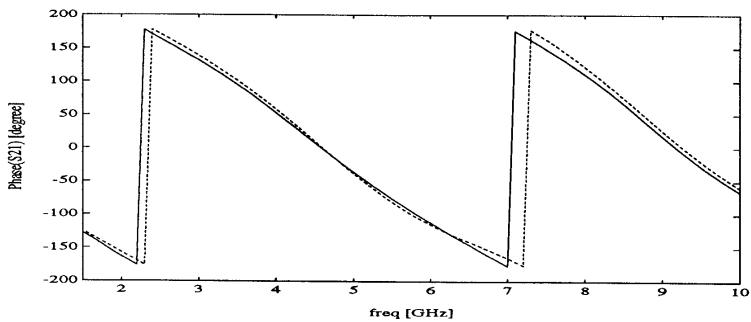


Figure 32. Phase of S_{21} of series single loop inductor.

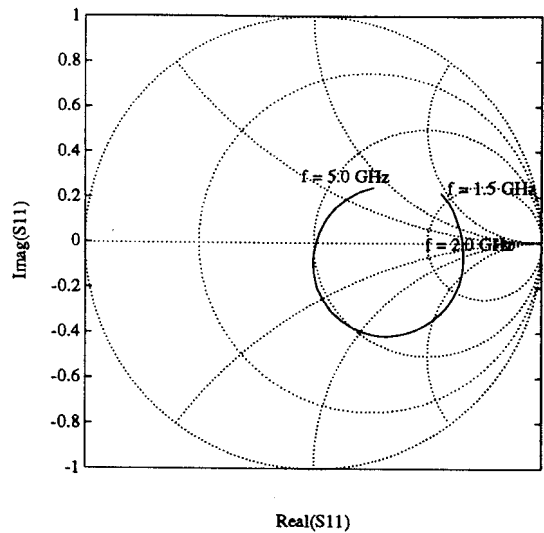


Figure 33. S'_{11} of series single loop inductor in Smith-chart format; reference planes shifted inwards by 10 mm.

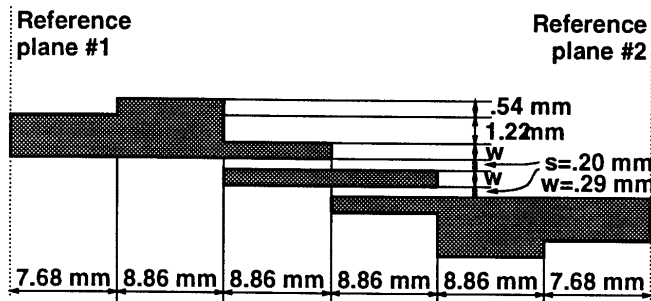


Figure 34. Two-section, coupled-line band-pass filter. Feed-line characteristic impedance is $50 \, \Omega$.

5.4 Parallel-coupled-line band-pass filter

Consider a two-section coupled-line filter, its layout shown in Figure 34. On parallel coupled lines, critical coupling occurs when the length of the coupler section becomes quarter-wavelength long. We obtain the dimensions shown in Figure 34 from the Super-Compact optimization routine, for a center frequency of 6 GHz and maximum

$|S_{21}|$ in the pass-band. Figures 35–38 present a comparison of Super-Compact (dotted line), experimental (dashed line) and our numerical results (solid line) for magnitude and phase of S_{11} and S_{21} . There is a good agreement among three traces, over the frequency range of 3 – 9 GHz.

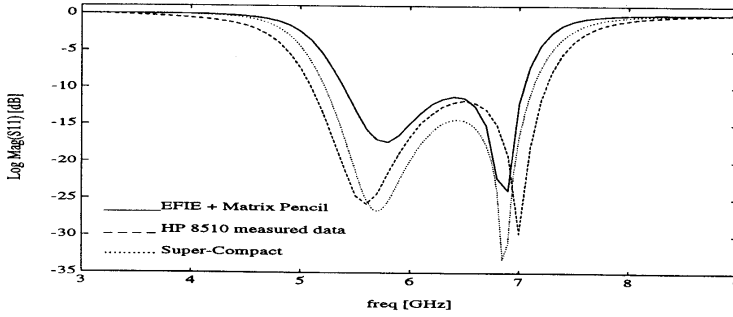


Figure 35. Magnitude of S_{11} of two-section, coupled-line, band-pass filter.

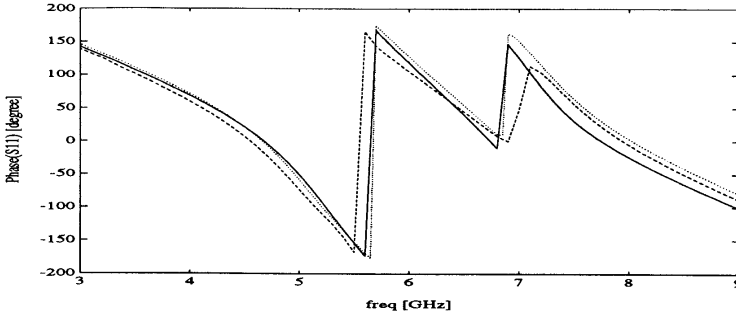


Figure 36. Phase of S_{11} of two-section, coupled-line, band-pass filter.

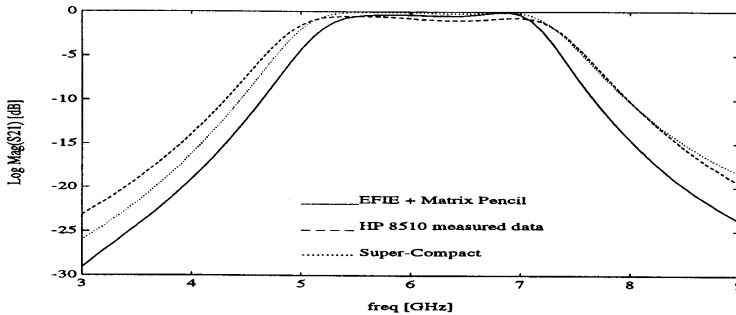


Figure 37. Magnitude of S_{21} of two-section, coupled-line, band-pass filter.

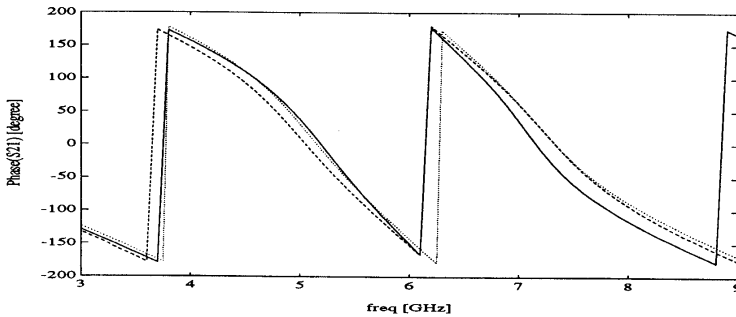


Figure 38. Phase of S_{21} of two-section, coupled-line, band-pass filter.

5.5 Two-port resonant structures

Our method can analyze arbitrarily shaped microstrip structures that consist of one or a multiple number of conducting patches. For the case of a multiple-patch structure, coupling among patches often exhibits resonant behavior. This is illustrated in the following examples.

5.5.1 Gap-coupled, half-wave filter

It is well known [47] that an open-circuited transmission-line section behaves as parallel resonant circuit in the frequency range where it is one-half wavelength long, or a multiple of half-wavelength long. Figure 39 shows such a section that is coupled to the input and output microstrip line, by means of the capacitance of the gap. Dimensions of the resonator are chosen to be one-half wavelength long at $f = 4$ GHz. Figures 40–43 show the S-parameters of this device. The solid-line trace represents results obtained by our numerical procedure, the dashed-line trace is measured on HP 8510B, dotted-line trace is obtained from Super-Compact model. The agreement among these three approaches is excellent.

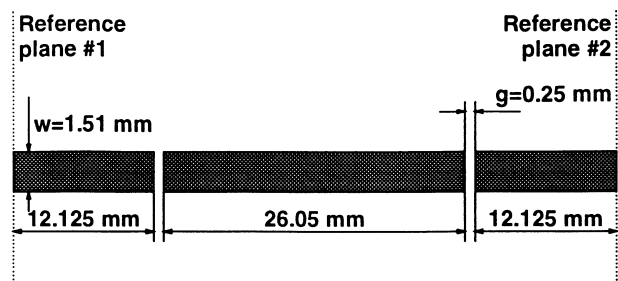


Figure 39. One-section, gap-coupled, half-wave filter. Feed-line characteristic impedance is $50\ \Omega$.

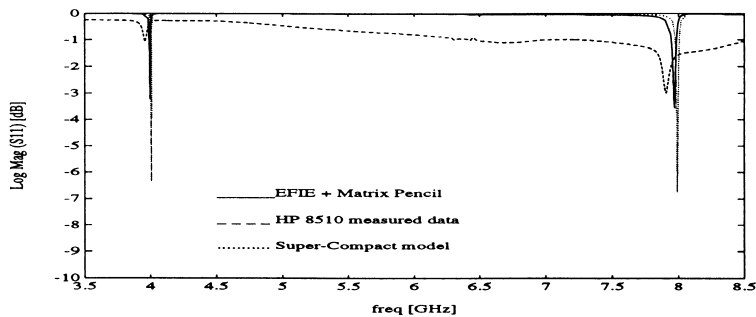


Figure 40. Magnitude of S_{11} of one-section, gap-coupled, half-wave filter.

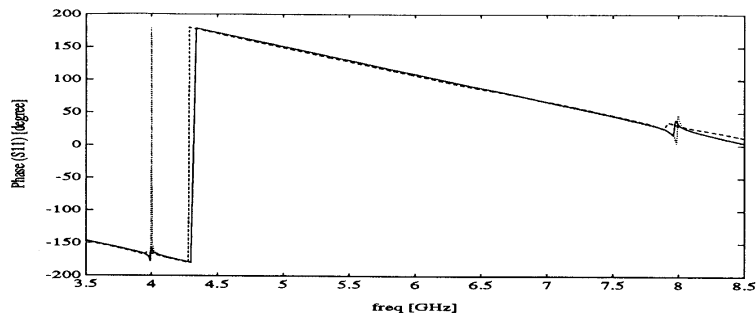


Figure 41. Phase of S_{11} of one-section, gap-coupled, half-wave filter.

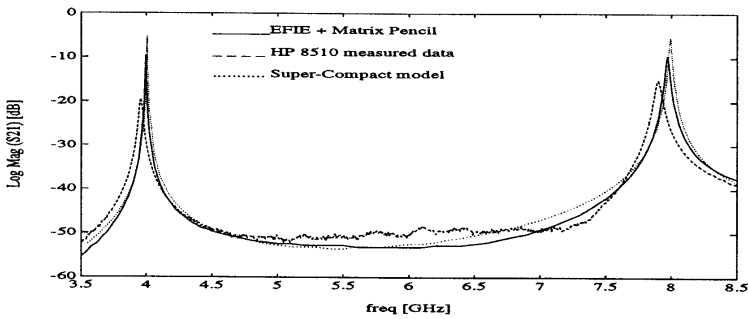


Figure 42. Magnitude of S_{21} of one-section, gap-coupled, half-wave filter.

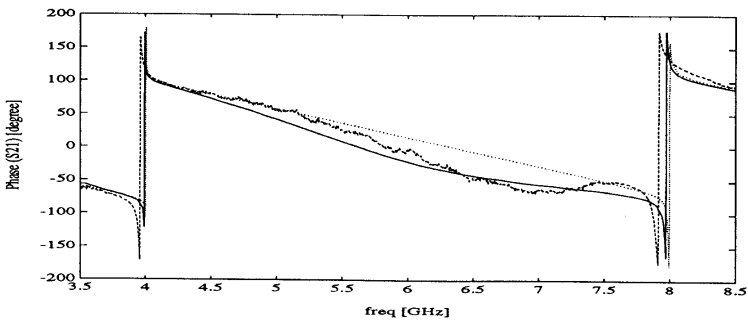


Figure 43. Phase of S_{21} of one-section, gap-coupled, half-wave filter.

5.5.2 Gap-coupled ring resonator disturbed by a notch

In case of the ring resonator, two degenerate modes occur at the resonance frequency. If the ring resonator is excited by symmetrical coupling lines, only one mode will be excited. Due to the orthogonality of degenerate modes, there will be no coupling between the two. However, if ring is coupled asymmetrically, or if a discontinuity is introduced in the ring, e.g., a notch, as illustrated in Figure 44, both modes are excited. What follows is the splitting of the resonance frequency [48]. As seen in Figures 45 and 46, our method clearly locates all cases of split resonance that are captured in measurements. (The vertical scale is linear).

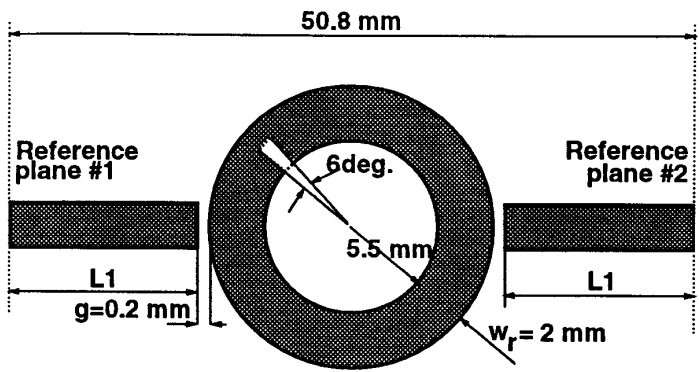


Figure 44. Gap-coupled ring resonator disturbed by a notch. Feed-line characteristic impedance is $50\ \Omega$.

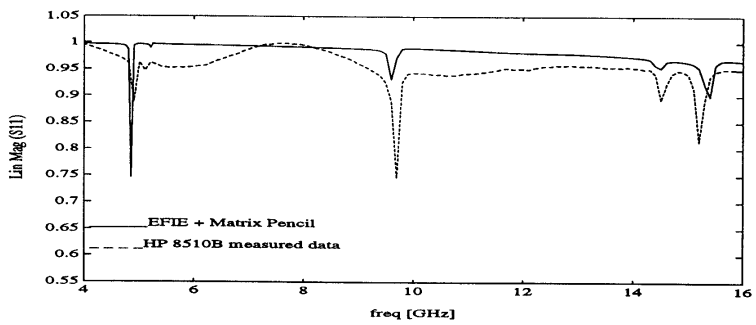


Figure 45. Magnitude of S_{11} of gap-coupled ring resonator disturbed by a notch.

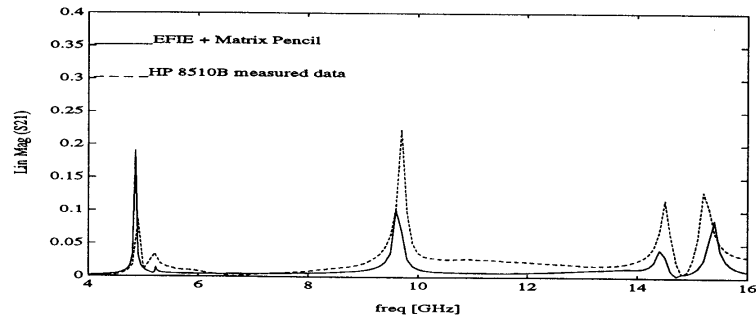


Figure 46. Magnitude of S_{21} of gap-coupled ring resonator disturbed by a notch.

5.6 Hybrid ring coupler (rat-race)

Since our method treats arbitrarily-shaped microstrip circuits with any number of ports, we also include a four-port example, a 180° hybrid ring coupler (rat-race).

Consider the hybrid ring shown in Figure 47. It acts as a 180° 3-dB coupler, since two outputs (ports 2 and 4) are in phase if port 3 is the input port, and 180° out of phase if port 1 is the input port. The hybrid ring coupler, or rat-race, is a narrow-band device. At the frequency of interest, ports 1 and 2, 2 and 3, and 3 and 4 are quarter-wavelength apart, while ports 1 and 4 separation is $3/4$ wavelength. Wave incident in port 3 splits equally into two waves on the ring traveling in opposite directions. They arrive in-phase to ports 2 and 4, while canceling each other at port 1. That decouples ports 1 and 3. The wave incident in port 1 also splits equally between ports 2 and 4, but the signals at ports 2 and 4 due to an excitation at port 1, are 180° out of phase, thus forming a 180° hybrid coupler. Ports 2 and 4 are also uncoupled, which follows from symmetry with respect to ports 1 and 3. The dimensions of the ring in Figure 47 are picked for a frequency of operation of 8.0 GHz, therefore we carry our analysis in the 4 – 12 GHz frequency range. Figures 48 to 50 show comparison between the numerical, Super-Compact, and experimental results for S_{11} , S_{21} and S_{31} parameters. From Figures 48 and 50, it follows that the center frequency is actually 7.8 GHz. As expected, ports 1 and 3 are uncoupled at this frequency (Figure 50), while ports 2 (as shown in Figure 49) and 4 are approximately 3 dB down with respect to port 1. From these figures, it follows that this structure actually behaves as a hybrid coupler in frequency range 7–9 GHz, which makes for $(9 - 7)/8 = 25\%$ relative bandwidth. We obtain experimental results (dashed line) by use of two-port de-embedding procedure described in section 5.1. However, the other two ports, that are terminated into matched loads, do reflect approximately -20 dB ($1/10$) of incoming signal, due to imperfections in the microstrip to coax connectors, versus -40 dB or less of desired reflected level. The main consequence is that the measured traces for four-port examples have an error term built-in, due to the two-port de-embedding procedure used on four-port networks.

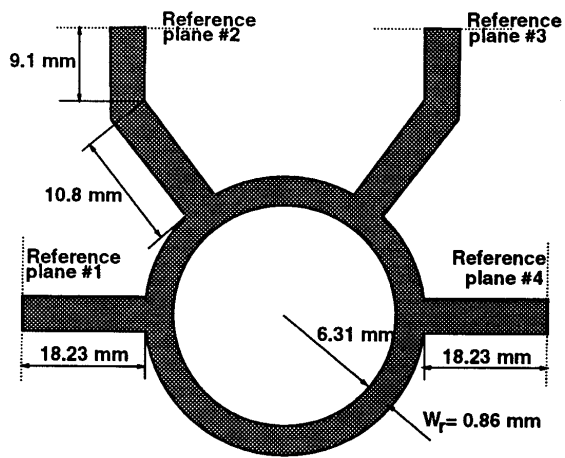


Figure 47. Hybrid ring coupler (rat-race). Feed-line characteristic impedance is $50\ \Omega$.

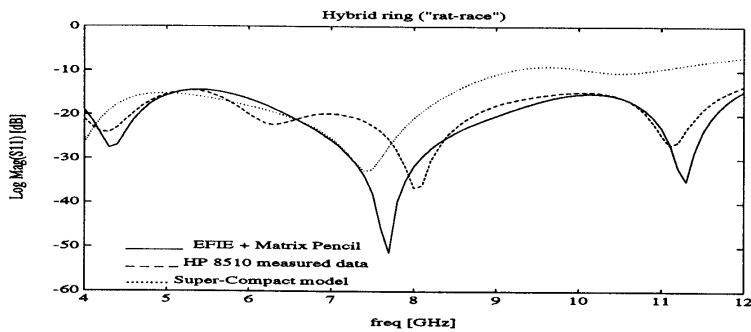


Figure 48. Magnitude of S_{11} of hybrid ring.

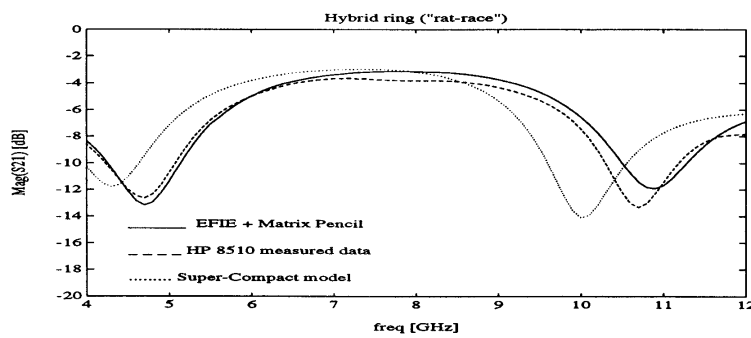


Figure 49. Magnitude of S_{21} of hybrid ring.

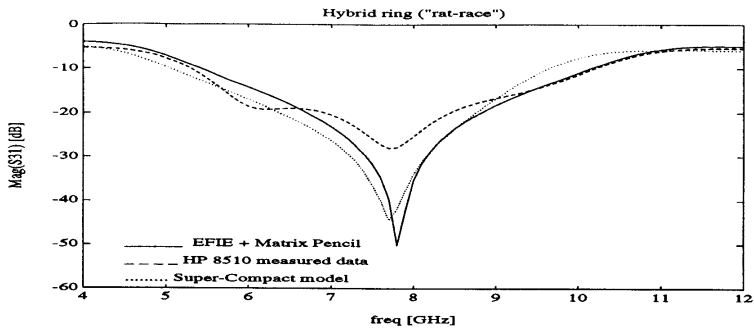


Figure 50. Magnitude of S_{31} of hybrid ring.

6. Conclusion

A dynamic approach for analysis of arbitrarily shaped, open microstrip structures was presented. With this, all types of radiation existing on the microstrip were taken into account. Use of the triangular basis functions in conjunction with the method of moments allowed for characterization of complex, arbitrarily shaped microstrip patches, over a broad range of frequencies. The Matrix Pencil method was used for decomposition of current along the microstrip lines into various modes, in addition to the numerical match-terminating condition, to solve for scattering parameters of the device under test.

We developed a powerful FORTRAN computer code, running on Sun Sparcstations and on IBM RISC 6000, and tested our method on a range of two-port and four-port microstrip devices. Our results were extensively compared to experimental results and other available data, and, for majority of examples, an overall very good agreement was found between our results and other data. Novel contributions of this work to the area of microstrip analysis and measurements are:

- application of the Matrix Pencil method to solving for the modes along the microstrip line
- numerical simulation of a match-terminated line by modifications to the method of moments matrix
- implementation of an accurate de-embedding technique to network analyzer measurements
- unique combination of theoretical, numerical and experimental work presented here.

7. Acknowledgement

We would like to express our thanks to Dr. Ulrich L. Rhode of Compact Software Inc. for providing us their software free of cost.

References

1. Grieg, D. D., and H. F. Engelmann, "Microstrip — a new transmission technique for the kilomegacycle range," *Proceedings of IRE*, Vol. 40, No. 12, 1644–1650, December 1952.
2. Djordjević, A., M. Baždar, G. Vitošević, T. Sarkar, and R. F. Harrington, *Scattering Parameters of Microwave Networks with Multiconductor Transmission Lines: Software and User's Manual*, Artech House, Norwood, MA, 1990.
3. Schneider, M. V., "Microstrip lines for microwave integrated circuits," *Bell System Technical Journal*, Vol. 48, 1421–1444, 1969.
4. Wheeler, H. A., "Transmission line properties of parallel wide strips by conformal mapping approximation," *IEEE Transactions on Microwave Theory and Techniques*, Vol. 12, 280–289, 1964.
5. Stinehelfer, H. E., "An accurate calculation of uniform microstrip transmission lines," *IEEE Transactions on Microwave Theory and Techniques*, Vol. 16, 439–444, 1968.
6. Silvester, P., "Tem properties of microstrip transmission lines," *Proc. IEE*, Vol. 115, 42–49, 1968.
7. Farrar, A., and A. T. Adams, "Computation of propagation constant for the fundamental and higher order modes in microstrip," *IEEE Transactions on Microwave Theory and Techniques*, Vol. 24, 456–465, 1976.
8. Yamashita, E., and R. Mittra, "Variational method for the analysis of microstrip lines," *IEEE Transactions on Microwave Theory and Techniques*, Vol. 16, 251–256, 1968.
9. Gupta, K. C., R. Garg, and I. J. Bahl, *Microstrip Lines and Slotlines*, Artech House, Norwood, MA, 1979.
10. Jain, O. P., V. Makios, and W. J. Chudobiak, "Coupled mode model of dispersion in microstrip," *Electron. Lett.*, Vol. 7, 405–407, 1971.
11. Schneider, M. V., "Microstrip dispersion," *Proc. IEEE*, Vol. 60, 144–146, 1972.

12. Getsinger, W. J., "Microstrip dispersion model," *IEEE Transactions on Microwave Theory and Techniques*, Vol. 21, 1, 34–39, January 1973.
13. Kompa, G., and R. Mehran, "Planar waveguide model for calculating microstrip components," *Electron. Lett.*, Vol. 11, 449–460, 1975.
14. Denlinger, E. J., "A frequency dependent solution for microstrip transmission lines," *IEEE Transactions on Microwave Theory and Techniques*, Vol. 19, No. 1, 30–39, January 1971.
15. Itoh, T., and R. Mittra, "Spectral domain approach for calculating dispersion characteristics of microstrip lines," *IEEE Transactions on Microwave Theory and Techniques*, Vol. 21, 496–498, 1973.
16. Jackson, R. W., and D. M. Pozar, "Full wave analysis of microstrip open-end and gap discontinuities," *IEEE Transactions on Microwave Theory and Techniques*, Vol. 33, No. 10, 1036–1042, October 1985.
17. Katehi, P. G., and N. G. Alexopoulos, "Frequency dependent characteristics of microstrip discontinuities in millimeter wave integrated circuits," *IEEE Transactions on Microwave Theory and Techniques*, Vol. 33, No. 10, 1029–1035, October 1985.
18. Jackson, R. W., "Full wave, finite element analysis of irregular microstrip discontinuities," *IEEE Transactions on Microwave Theory and Techniques*, Vol. 37, No. 1, 81–89, January 1989.
19. Lewin, L., "Radiation from discontinuities in stripline," *Proceedings of the IEE*, Vol. H-107, 163–170, 1960.
20. Gardiol, F. E., *Introduction to Microwaves*, Artech House, Dedham, MA, 1984.
21. Wait, J. R., "Fields of a horizontal dipole over a stratified anisotropic half-space," *IEEE Transactions on Antennas and Propagation*, Vol. 14, 790–792, 1966.
22. Wait, J. R., *Electromagnetic Waves in Stratified Media*, Pergamon Press, New York, 1970.
23. Uzunoglu, N. K., N. G. Alexopoulos, and J. G. Fikioris, "Radiation properties of microstrip dipole," *IEEE Transactions on Antennas and Propagation*, Vol. 27, 853–858, 1979.
24. Mosig, J. R., and F. E. Gardiol, "General integral equation formulation for microstrip antennas and scatterers," *IEE, Proc. H, Microwave, Opt., Antennas*, Vol. 132, 175–182, December 1985.

25. Kong, J. A., *Theory of Electromagnetic Waves*. John Wiley and Sons, New York, 1975.
26. Kong, J. A., editor, *Research Topics in Electromagnetic Wave Theory*, Wiley, New York, NY, 1981.
27. Mosig, J. R., and T. K. Sarkar, "Comparison of quasistatic and exact electromagnetic fields from a horizontal electric dipole above a lossy dielectric backed by an imperfect ground plane," *IEEE Transactions on Microwave Theory and Techniques*, Vol. 34, No. 4, 179–187, April 1986.
28. Harrington, R. F., *Field Computation by Moment Methods*, R. E. Krieger, Malabar, FL, 1987.
29. Sarkar, T. K., P. Midya, Z. A. Marićević, M. Kahrizi, S. M. Rao, and A. R. Djordjević, "Analysis of arbitrarily shaped microstrip patch antennas using the sommerfeld formulation," *International Journal of Microwave and Millimeter-Wave Computer-Aided Engineering*, Vol. 2, No. 3, 168–177, 1992.
30. Rao, S. M., D. Wilton, and A. Glisson, "Electromagnetic scattering by surfaces of arbitrary shape," *IEEE Transactions on Antennas and Propagation*, Vol. 30, 409–418, 1982.
31. Rao, S. M., "Electromagnetic scattering and radiation of arbitrarily shaped surfaces by triangular patch modeling," Ph.D. Thesis, University of Mississippi, 1980.
32. Hua, Y., and T. K. Sarkar, "Generalized pencil-of-functions method for extracting the poles of an electromagnetic system from its transient response," *IEEE Transactions on Antennas and Propagation*, Vol. 37, No. 2, 229–234, February 1989.
33. Hua, Y., and T. K. Sarkar, "Matrix pencil method for estimating parameters of exponentially damped/undamped sinusoids in noise," *IEEE Transactions on Acoustics, Speech and Signal Processing*, Vol. 38, No. 5, 814–824, May 1990.
34. Hua, Y., "On techniques for estimating parameters of exponentially damped/undamped sinusoids in noise," Ph.D Thesis, Syracuse University, 1988.
35. Menzel, W., "A new traveling-wave antenna in microstrip," *AEU Electronics and Communications Journal*, Vol. 33, No. 4, 137–140, April 1979.
36. Oliner, A. A., "Leakage from higher modes on microstrip line with application to antennas," *Radio Science*, Vol. 22, No. 6, 907–912, November 1987.

37. Oliner, A. A., and K. S. Lee, "Scannable millimeter wave arrays; chapter ix: Microstrip line leaky-wave strip antennas," Technical report, Polytechnic University Weber Research Institute, 1988.
38. Harrington, R. F., *Time-Harmonic Electromagnetic Fields*. McGraw-Hill, New York, NY, 1987.
39. Mosig, J. R., and F. E. Gardiol, "A dynamical radiation model for microstrip structures, *Advances in Electronics and Electron Physics*, Vol. 39, 139–237, 1982. P. Hawkes Ed., Academic Press, New York.
40. Itoh, T., editor, *Numerical Techniques for Microwave and Millimeter-Wave Passive Structures*. John Wiley & Sons, New York, NY, 1989.
41. Wadell, B. C., *Transmission Line Designer's Handbook*, B. C. Wadell, September 1989.
42. Ermert, H., "Guided modes and radiation characteristics of covered microstrip lines," *AEU Electronics and Communications Journal*, Vol. 30, No. 1, 65–70, January 1976.
43. Chang, D. C., and E. F. Kuester, "Total and partial reflection from the end of a parallel-plate waveguide with an extended dielectric loading, *Radio Science*, Vol. 16, No. 1, 1–13, January 1981.
44. Gronau, G., "Scattering-parameter measurement of microstrip devices," *Microwave Journal*, Vol. 35, No. 11, 82–92, November 1992.
45. Gronau, G., and I. Wolff, "A simple broad-band device deembedding method using an automatic network analyzer with time-domain option, *IEEE Transactions on Microwave Theory and Techniques*, Vol. 37, No. 3, 479–483, March 1989.
46. Hewlett-Packard Company, *HP 8510B Network Analyzer — Operating and Programming Manual*, July 1987.
47. Collin, R. E., *Foundations For Microwave Engineering*, McGraw-Hill, New York, NY, second edition, 1992.
48. Wolff, I., "Microstrip bandpass filter using degenerate modes of a microstrip ring resonator," *Electronics Letters*, Vol. 8, No. 12, 302–303, June 1972.